Dynamic single-cell RNA sequencing reveals BCG vaccination curtails SARS-CoV-2 induced disease severity and lung inflammation

Alok K. Singh[1,*], Rulin Wang[2,*], Kara A. Lombardo[3], Monali Praharaj[4], C. Korin Bullen[1], Peter Um[1], Stephanie Davis[1], Oliver Komm[1], Peter B. Illei[5], Alvaro A. Ordonez[6], Melissa Bahr[6], Joy Huang[1], Anuj Gupta[2], Kevin J. Psoter[7], Sanjay K. Jain[6], Trinity J. Bivalacqua[8], Srinivasan Yegnasubramanian[2,**], William R. Bishai[1,**]

[1]Johns Hopkins University, School of Medicine, Department of Medicine, Center for Tuberculosis Research, Baltimore, MD, USA

[2]Sydney Kimmel Comprehensive Cancer Center at Johns Hopkins, Baltimore, MD, USA

[3]Johns Hopkins University, School of Medicine, Department of Urology, Baltimore, MD, USA

[4]Bloomberg~Kimmel Institute for Cancer Immunotherapy at Johns Hopkins, Baltimore, MD, USA

[5]Johns Hopkins University, School of Medicine, Department of Pathology, Baltimore, MD, USA

[6]Johns Hopkins University, School of Medicine, Department of Pediatrics, Division of Infectious Diseases, Baltimore MD, USA

[7]Johns Hopkins University, School of Medicine, Department of Pediatrics, Division of General Pediatrics, Baltimore, MD, USA

[8]Perelman School of Medicine at the University of Pennsylvania, Division of Urology, Department of Surgery, Philadelphia, PA, USA

*Contributed equally

Correspondence: ** Joint corresponding authors

William R. Bishai, MD, PhD
JHU School of Medicine
CRB2, Room 108
1550 Orleans Street
Baltimore, MD 21287
e-mail: wbishai@jhmi.edu

Srinivasan Yegnasubramanian
JHU School of Medicine
CRB2, Room 145
1550 Orleans Street
Baltimore, MD 21287
e-mail: syegenasu@jhmi.edu

Abstract:

COVID-19 continues to exact a toll on human health despite the availability of several vaccines. Bacillus Calmette Guérin (BCG) has been shown to confer heterologous immune protection against viral infections including COVID-19 and has been proposed as vaccine against SARS-CoV-2 (SCV2). Here we tested intravenous BCG vaccination against COVID-19 using the golden Syrian hamster model together with immune profiling and single cell RNA sequencing (scRNAseq). We observed that BCG reduced both lung SCV2 viral load and bronchopneumonia. This was accompanied by an increase in lung alveolar macrophages, a reversal of SCV2-mediated T cell lymphopenia, and reduced lung granulocytes. Single cell transcriptome profiling showed that BCG uniquely recruits immunoglobulin-producing plasma cells to the lung suggesting accelerated antibody production. BCG vaccination also recruited elevated levels of Th1, Th17, Treg, CTLs, and Tmem cells, and differentially expressed gene (DEG) analysis showed a transcriptional shift away from exhaustion markers and towards antigen presentation and repair. Similarly, BCG enhanced lung recruitment of alveolar macrophages and reduced key interstitial macrophage subsets, with both cell-types also showing reduced IFN-associated gene expression. Our observations indicate that BCG vaccination protects against SCV2 immunopathology by promoting early lung immunoglobulin production and immunotolerizing transcriptional patterns among key myeloid and lymphoid populations.

Introduction:

COVID-19, the current global pandemic caused by the novel coronavirus SARS-CoV-2 (SCV2), has precipitated a severe health and economic crisis worldwide, dramatically affecting the lives of billions of people across all continents. Despite the widespread use of vaccines since December 2020, the limited efficacy of certain licensed vaccines and the development of novel SCV2 variants capable of breakthrough infections in vaccinated individuals poses a continuing public health threat (1,2). Further, there are indications that SCV2 and future variant coronaviruses may never be fully eliminated, and thus repetitive vaccination campaigns with updated vaccines may be necessary as occurs with influenza (3,4).

SCV2 infection of ACE2 and TMPRSS2 expressing airway epithelial cells results in pyroptotic cell death and the subsequent release of infectious viral particles, damage-associated molecules (DAMPS), and inflammation inducing IL1-β (5,6). The release of DAMPs and viral particles and their sensing by epithelial cells and alveolar macrophages results in a local exaggerated proinflammatory immune response primarily driven by cytokines (IL-6 and IFN-γ) and chemokines (CCL2 and CXCL10) (7). This is followed by infiltration of monocytes, natural killer (NK) cells and lymphocytes from the peripheral blood to infected tissues causing even more pronounced inflammation eventually causing organ damage in individuals with severe disease (7). Longitudinal studies in infected individuals during the active and recovery phases of the disease have revealed that early host immune responses are dominated by cells of innate immune system, including neutrophils, monocytes, plasmacytoid dendritic cells (pDCs), and NK cells (8,9), while adaptive immune response are important for viral clearance and development of long term T and B cell memory responses (10).

Because BCG has been shown to impart heterologous immunity and to protect against viral infections (11,12), a number of human clinical trials evaluating BCG for protection against COVID-19 were launched in early 2020. One such study now reports that indeed BCG vaccination

reduces the risk of COVID-19 diagnoses by as much as 68% compared to unvaccinated controls (13). BCG is also a well-known vaccine adjuvant and has been shown to boost immunogenicity of protein subunit, DNA, and viral vectored vaccines in pre-clinical models (14-16). Hence further studies of BCG as a COVID-19 vaccine either alone or in combination with the current arsenal of specific anti-COVID-19 vaccines may be warranted.

BCG has been shown to reprogram both myeloid cells and NK cells through processes collectively termed “trained immunity”. BCG is rapidly phagocytosed by macrophages and has been shown to elicit both epigenetic and metabolomic modifications that elevate their immune setpoint upon re-challenge with a heterologous antigens including viruses (17,18). Upon re-challenge with heterologous antigens, BCG-trained macrophages show elevated cytokine release and demonstrate reprogramming towards M1-like phenotypes. These initial events are associated with heterologous B and T-lymphocyte activation, elevated antibody titers (19) and expansion of unconventional T cells such as innate lymphoid cells (ILCs) and mucosa-associated invariant T (MAIT) cells (20,21). BCG exposure also leads to expanded “trained” populations of hematopoietic stem cells (HSCs) and multipotent progenitors (MPPs) in the bone marrow that confer enhanced protection against subsequent pathogen challenges (22).

Randomized control studies of BCG vaccination in humans have demonstrated improved control of live attenuated yellow fever virus (23), live-attenuated influenza A (H1N1) (24), and human papilloma virus (25). Furthermore, animal studies have similarly demonstrated a BCG benefit against at least eight viruses including two positive-sense, single-stranded RNA viruses (Cardiovirus A and Japanese encephalitis virus, neither of which is closely related to coronaviruses) (17,26,27). Two recent reports show that subcutaneous BCG does not protect in mouse models of SCV2 infection (28,29), but that intravenous BCG does confer protection in mice (29). A recent hamster study showed that both subcutaneous and intravenous BCG vaccination were ineffective in SCV2 disease prevention (30). These prior studies did not evaluate the

104 comprehensive cellular immune landscape using robust, global immune profiling transcriptomic
105 tools such as single cell RNA sequencing (28-30).

106 In this study, we employed the non-lethal, self-resolving golden Syrian hamster model to
107 evaluate the ability of intravenous BCG to protect against SCV2. We evaluated its impact on lung
108 viral titers, tissue pathology using histopathology, immunohistochemistry (IHC) and PET/CT
109 (positron emission tomography/computed tomography), and cell populations by flow cytometry
110 and single-cell RNA sequencing (scRNAseq). Our results reveal that BCG-vaccinated animals
111 had significantly reduced viral loads and tissue pathology, reduced lung T cell lymphopenia, and
112 a significant reprogramming of myeloid cell subsets. Moreover, we observed that during SCV2
113 infection BCG uniquely recruits immunoglobulin-producing plasma cells to the lung suggesting
114 accelerated antiviral antibody production. BCG vaccination also resulted in elevated levels of
115 several types of lung $CD4^+$ T cells (Th1, Th17, Treg, CTLs, and Tmem), and these cells showed
116 modified transcriptional programs towards antigen presentation and away from exhaustion.
117 Similarly, BCG enhanced lung recruitment of alveolar macrophages and reduced key interstitial
118 macrophage subsets with both cells also showing reduced IFN-associated gene expression. Our
119 results indicate that BCG vaccination has a tolerizing effect on SCV2-mediated lung inflammation
120 and that it may accelerate antiviral antibody responses.
121
122
123 **Results:**

124 **BCG vaccination reduces viral load and lung pathology and alters lung immune cell**
125 **infiltration in SCV2-infected hamsters**. We set out to determine whether prior BCG vaccination
126 alters the course of SCV2 infection in the golden Syrian hamster model (**Fig. 1A**) which has
127 previously been shown to exhibit a self-resolving, and non-lethal form of COVID-19. We evaluated
128 lung histopathologic changes at D4 and D7 post SCV2 challenge with and without prior BCG
129 vaccination. As shown in **Fig. 1B-C**, bronchopneumonia was present in 100% of unvaccinated

hamsters on both D4 and D7 but was absent in all BCG-vaccinated hamsters on D4 and found in only 25% on D7. Similarly, 100% of unvaccinated hamsters showed neutrophilic infiltration at D4 while only 50% of BCG-vaccinated hamsters showed this finding (**Fig. 1D**). In contrast BCG vaccination showed a trend for increased macrophage infiltration (80% at D4) while only 60% of unvaccinated animals showed this finding (**Fig. 1E**). Regarding the well-described SCV2-mediated lymphopenia, BCG vaccination was able to partially correct infiltrating lung lymphocytes with BCG-vaccinated hamster lungs also showing significantly higher levels of lung lymphocytes (CD3 positivity) both by traditional histology and immunohistochemistry (**Fig. 1F, Fig. S1A**), and this was true for perivascular lymphocytic infiltration as well (**Fig. S1B**). As expected, all BCG vaccinated hamsters showed granuloma formation, a phenomenon that was uniformly absent in unvaccinated animals (**Fig. S1C)**. Thus, prior BCG vaccination reduced SCV2-induced bronchopneumonia with its concomitant neutrophilic infiltration while simultaneously preventing lung lymphopenia and enhancing lung macrophage levels.

We also evaluated the effect of BCG vaccination on lung viral load by measuring infectious viral particles ($TCID_{50}$) and viral RNA in lung homogenates. We observed a significant decrease in $TCID_{50}$ in BCG vaccinated animals at D4 **(Fig. 1G)**, and a trend of reduced viral mRNA (**Fig. 1H**) at this same time point. $TCID_{50}$ and viral mRNA levels were significantly lower at D7 compared to D4 and levels BCG-vaccinated animals did not differ from the unvaccinated ones likely because of progressive disease resolution in both groups.

BCG vaccination blunts SCV2-mediated lung T cell lymphopenia, enhances macrophage lung recruitment, and reduces lung infiltration by granulocytes. To assess overall cell population fluxes in hamster lungs, we performed multicolor flow cytometry. We found that lung T cell infiltration ($CD3^+$ cells) was dramatically boosted by BCG vaccination in the absence of SCV2 (45% of live cells) compared to age-matched healthy animals (18%) (**Fig. 2A**). In unvaccinated animals challenged with SCV2, the total lung $CD3^+$ population was reduced at D4 and D7 to 4-

6%; while BCG vaccinated, SCV2 challenged animals showed a trend to have nearly twice as many $CD3^+$ cells (10-12%) at these same time points (**Fig 2A**) supporting our histopathological observations. This same effect of BCG preventing T cell depletion in the lung was present to an even greater extent among lung $CD4^+$ T cells (**Fig. 2B**). We did not observe this same pattern in hamster spleens suggesting that the observed effects of BCG vaccination were limited to the site of active infection in the lungs (**Fig. S2 A-B**). Similarly, BCG vaccination in the absence of SCV2 infection prompted a pronounced macrophage recruitment to the lung (55% of live cells) compared to healthy (unvaccinated) animals (5%) (**Fig. 2C**). And while SCV2 infection led to a modest macrophage lung recruitment by D7 (12% of live cells), previously BCG vaccinated animals showed significantly elevated macrophage populations in the lungs (30% of live cells) on both D4 and D7 **(Fig. 2C)**. In contrast, for granulocytes, we found that SCV2-challenged, unvaccinated hamster lungs revealed dramatic infiltration by polymorphonuclear leukocytes (PMNs) on D4 (80% of live cells) and D7 (72%) (**Fig. 2D**) in accordance with the profound bronchopneumonia observed **(Fig. 1B-C)**. Pre-vaccination with BCG had the effect of limiting the SCV2 mediated granulocytic infiltration to levels of 30% on D4 and 32% on D7 which were levels essentially equivalent to those in the lungs of vaccinated, unchallenged hamsters. A modest increase in macrophages at both D4 and D7 in the splenic compartment, not statistically significant, was observed in BCG-vaccinated, SCV2-infected animals compared to unvaccinated SCV2 infected animals (**Fig. S2C**). Splenic granulocytes trended to be lower in BCG vaccinated animals compared to unvaccinated animals (**Fig. S2D)**, similar to the observations in the lungs.

Single cell transcriptional profiling in lung cells in BCG vaccinated and unvaccinated hamsters. To obtain a higher resolution of pulmonary immune responses linked to BCG immunization during SCV2 infection, hamster lungs were examined using droplet-based single cell RNA sequencing (10X Genomics) during the peak (day 4) and resolution (day 7) phases of COVID-19. BCG-vaccinated, unchallenged hamster lungs were also studied. A total of 13

hamsters were evaluated in the following three groups: BCG vaccination only (3 animals), SCV2 infection only (2 animals on D4; 2 on D7), and BCG vaccination with SCV2 challenge (3 animals on D4; 3 on D7). Sequencing was performed in a total of 194,536 cells, and after filtering out low-quality cells, red blood cells, and doublets 112,928 cells were analyzed. (**Table S1**). The mean number of cells analyzed per animal in BCG vaccinated lungs, SCV2 infected lungs and BCG-vaccinated + SCV2 infected lungs was 11,249, 8,643, and 7,434 respectively.

BCG reverses lymphopenia, macrophage depletion, and loss of structural cell types due to SCV2 infection. By graph-based clustering of uniform manifold approximation and projection (UMAP), transcriptomes of 17 major cell types or subtypes were identified in hamster lungs **(Table S2)**. These included lymphoid, myeloid, and non-immune cell types (**Fig 3A-C**). These cell clusters were relatively homogenously distributed across all animal lungs at both timepoints and were based on the expression of well-defined canonical genes as shown in **Fig. 3D.** The 5 most highly expressed genes in each cluster are shown in **Fig. S3**.

BCG expands Th1, Th17, Treg, CTLs, Tmem, and plasma cell populations during SCV2-infection. Next, we performed subset analyses to evaluate lung immune cells during SCV2 infection in vaccinated and unvaccinated hamsters. We were able to identify 10 distinct lymphocyte cell types (**Fig. 4A, S4A-B**). Among the $CD4^+$ T cells in hamster lungs, we were able to distinguish Th1, Th17, Treg (regulatory T cells) and Tmem (memory T cells) cells primarily based on *Ifng*, *Itgb7*, *Foxp3*, and *Lef1* expression, respectively (**Fig. S4C-D**). CTLs (cytotoxic T cells) showed high *Gzmk* and *Gzma* but low *Cd4* expression. Plasma cells were identified by their elevated expression of *Jchain* and *Mzb1* (**Fig. S4C-D**). As may be seen in **Fig. 4A**, both at D4 and D7 post-SCV2 challenge, hamsters that were BCG-vaccinated maintained high levels of Th1, Th17, Treg, CTLs, Tmem, and plasma cells in their lungs. With the exception of plasma cells, vaccination with BCG only (no SCV2 challenge) stimulated high levels of these cell types in

the lungs, and these relatively high levels were maintained in hamsters challenged with SCV2. In contrast, a plasma cell response was not observed in BCG-vaccinated, unchallenged animals; rather elevated plasma cell numbers in the lungs were uniquely observed only in BCG-vaccinated, SCV2 infected animals.

Elevation of plasma cell abundance in BCG-vaccinated, SCV2 challenged hamsters. In order to estimate the numbers of lymphocytes in healthy control hamsters, we were able to compare our scRNAseq cell abundance data with previously published data which included healthy hamster controls (31) (**Fig. S5A**). Both Th1 and Treg lymphocytes were scarce in the lungs of healthy hamsters but were strongly recruited to the lung by BCG vaccination both in the presence and absence of SCV2 challenge (**Fig. S5B**). Plasma cells were not seen abundantly in either healthy hamster lungs or unchallenged, BCG-vaccinated hamsters. Thus, an enhanced plasma cell response occurred only in the presence of prior BCG-vaccination followed by SCV2 challenge **(Fig. 4A)**. Moreover, an evaluation of gene signatures revealed elevated expression of immunoglobulin production by plasma cells in BCG-vaccinated and SCV2 challenged animals strongly suggesting that these plasma cells appear functionally active in antibody production (**Fig. 4B**).

Lung CD4$^+$ Th1 cells showed reduced exhaustion and mitochondrial stress gene signatures with BCG vaccination. By gene signature and gene ontology (GO) analysis, we found that Th1 cells in unvaccinated, SCV2-challenged showed evidence exhaustion markers (**Fig 4C**) and a high degree of mitochondrial respiratory gene expression and translation (**Fig 4D**), consistent with mitochondrial dysfunction in T cells that have been previously reported (32). In contrast, in Th1 cells from BCG-vaccinated, SCV2 challenged animals, pathways related to T cell activation, T cell immunity, and antigen processing were upregulated suggesting greater functional immunity (**Fig. 4E**).

Differentially expressed genes (DEGs) in lung CD4 Th1 cells: When we considered specific DEGs in Th1 cells in BCG-vaccinated, SCV2-challenged hamsters (**Fig 4F,G**), we found strong upregulation of genes associated with protection from injury. These include *Cd74,* a gene recently associated with antiviral responses and protection from lung injury (33,34), *Cd70* a gene associated with T cell activation, *Ltb* (lymphotoxin-beta) a gene known to play a protective role in other viral infection, *Gsdma* (gasdermin A) which has been found to be deficient in autopsy studies of humans with severe COVID-19 (35), and *Ifng* (IFN-γ) a prominent Th1 activator. Several of these same genes including *Cd74*, *Ltb*, and *Gsdma* were also strongly expressed in Th17 and Treg lung lymphocytes from BCG-vaccinated, SCV2-challenge hamsters (**Fig. 4H-I**).

In contrast, in Th1 cells from non-vaccinated, SCV2-challenged hamsters, we found DEGs that were associated with markers of exhaustion and ongoing viral infection (**Fig. 4F,G**). Markers of exhaustion included *Cd278* (*Icos*), a gene known to be up-regulated in SCV2 (36), *Ctla4*, a marker found in human SCV2 convalescent plasma (37), and *Tnfrsf18* (GITR). Genes associated with ongoing viral infection included *Ifitm2* (IFN-induced transmembrane protein 2) which has recently been shown to be hijacked by SCV2 and to promote ongoing infection response (38), *Bzw2* (Basic Leucine Zipper and W2 Domain-Containing Protein 2) (39) which is a viral restriction factor shown to interact with the SCV2 M protein, and IFN-responsive regulatory proteins *Mx1* (an IFN induced GTP-binding protein), *Rgs10* (Regulator of G protein signaling-10), and *Irf7* which is known to be involved in transcription activation of viral-inducible cellular genes and is a gene for which polymorphisms known to be associated with severe SCV2 (40).

Myeloid cell changes mediated by BCG vaccination: enhanced AM abundance and diminished IM lung recruitment. Our scRNAseq analysis of myeloid cells revealed 10 distinct myeloid cell subsets (**Fig. 5A, Fig. S6A-B**). Alveolar macrophages (AMs) are relatively

immunotolerant cells that scavenge debris and play an important role in pathogen clearance (41). We identified two clusters of AMs, the first identified by the classic AM marker *Siglecf* (Siglecf+ AMs) and the second identified by the presence of the scavenger receptor *Marco* (Marco+ AMs). BCG vaccination has been shown to induce recruitment of Siglecf+ AMs to the lung in healthy human volunteers (42), and consistent with this, while we observed virtually no Siglecf+ AMs in healthy hamster lungs, this population was strongly induced by BCG vaccination (**Fig. S5C**). In contrast, scavenging Marco+ AMs were present in high numbers in healthy hamster lungs, and BCG vaccination caused ~2-fold increased in this population (**Fig. S5C**). Unvaccinated, SCV-infected hamsters showed a high degree of depletion of both categories of AMs, but prior BCG vaccination served to prevent the loss of both AMs from the lung (**Fig 5A, S5C**).

Interstitial macrophages (IM) are more inflammatory than AMs and are recruited from the periphery during lung infection (43,44). In addition to traditional IMs, we identified a second population which strongly expressed *Isg15* (Isg15+ macrophages) indicating that they are highly responsive to IFN I and hence likely to be hyperinflammatory. Both IMs and Isg15+ macrophages were virtually absent in healthy hamster lungs (**Fig. S5C**) and in unvaccinated hamsters, but both of these cell types were recruited to the lungs in high numbers following SCV2 challenge. Interestingly, prior BCG-vaccination significantly blunted this recruitment (**Fig 5A, S5C**). In keeping with the inflammatory nature of Isg15+ macrophages, we observed that SCV2 infection caused a strong upregulation of *Ccr5*, *Ccl8*, *Ccl7*, *Ccl5*, *Ccl4*, *Ccl2* and *Cxcl10* in IFN-I-responsive Isg15+ macrophages (**Fig. 5B**). These inflammatory chemokines remained at basal expression levels in either BCG vaccinated animals or those challenged with SCV2 after vaccination. These observations support the notion that BCG vaccination leads to an elevated setpoint of scavenging AM in the lungs, but during SCV2 infection it prevents excess recruitment of pro-inflammatory Isg15+ macrophages and IMs which may be involved in SCV2-mediated, lung immunopathology.

Dendritic cells (DCs). We observed an increase in dendritic cells following SCV2 infection at both time points. In contrast, levels of DCs remained essentially undetectable with BCG vaccination alone or BCG-vaccination in the presence of SCV2 challenge (**Fig 5A**). Patients with severe COVID-19 demonstrate reduced DC levels in blood possibly because of recruitment to infection sites (45). DCs, especially pDCs, are considered a chief source of IFN I, a cytokine which is found at unusually low levels during human COVID-19 suggesting that DCs have an exhaustion phenotype during SCV2 infection (46,47).

Myeloid-derived suppressor cells (MDSCs). Expansion of MDSCs have been described in humans with severe COVID-19, a phenomenon that correlates with lymphopenia and enhanced arginase activity, while milder forms of disease display a reduced MDSCs count (48,49). Increased recruitment of both G-MDSCs and M-MDSCs subtypes of myeloid cells are reported in COVID-19 patients and may contribute to acute respiratory distress syndrome (ARDS) (50,51). BCG vaccination led to reductions of in both M-MDSCs and G-MDSCs among SCV2-challenged hamsters suggesting a protective effect (**Fig. 5A**). The majority of G-MDSCs identified in our data showed marked elevation of *Il1b* and *Arg1* both strong biomarkers of COVID-19 severity (51) (**Figure S3**).

Myeloid cell DEGs reveal divergent immune programs. Next, we evaluated DEGs in Siglecf+ AM, Marco+ AM, IMs, Isg15+ macrophages, and M-MDSCs. In unvaccinated animals infected with SCV2, there was high transcription of IFN-α (IFN-I) response genes (**Fig 5C**); these included *Isg15*, *Irf7*, and *Mx1* as well as chemokine-encoding genes such as *Ccl2*, *Ccl12*, and *Ccl4* and those associated with lymphocyte activation (*Slamf9*) all consistent with ongoing inflammatory responses (**Fig. 5C-D**). However, in vaccinated animals challenged with SCV2, the predominant DEGs were shifted towards those involved in metabolic and repair processes such as *Ubd* (encoding ubiquitin), *Ppa1* (encoding pyrophosphatase 1), *Cdo* (encoding cysteine dioxygenase)

or genes for complement factor expression (*C1qa*, *C1qc*) as might be expected in a less inflammatory, repair-oriented environment (**Fig. 5C-D**). Focused analysis of IFN-α and IFN-γ response gene signature scores revealed that for major myeloid cell subsets, BCG-vaccinated animals showed reduced expression of these interferons (**Fig. 5C**), including for Isg15+ macrophages which had the highest levels of IFN-γ expression**.**

DEGs in Isg15+ macrophages. In unvaccinated, SCV2-challenged Isg15+ macrophages we observed robust upregulation of type I IFN-dependent ISGs (interferon-stimulated genes), (*Bst2, Mxd1* and *Ifitm2*), ISGs known to be activated following viral genome sensing (*Irf7*, *Fcgr4*, *Slamf9*, and *Irf9),* antiviral restriction factors (*Apobec1),* and inflammatory mediators known to drive COVID-19 severity (*Ccl2*, *Ccl4*, *Ccl7*, *Ccrl*2, *Cxcl10*, and *Ccl12*) **(Fig. 5D)**. In contrast, Isg15+ macrophages among BCG-vaccinated, SCV2-challenged hamsters expressed high levels of oxidative phosphorylation genes including *Atp5*, *Atp5c1*, *Atp5f1a* and *Atp5g3* as well as mitochondrial *Chchd10* (a gene predicted to be involved in mitochondrial oxidative phosphorylation) suggesting upregulated oxidative phosphorylation, a characteristic hallmark of BCG training (52). Isg15+ macrophages among BCG-vaccinated animals showed increased expression of mitochondrial genes *Suclg1* (succinyl-CoA ligase), and *Sdhd* (succinate dehydrogenase) suggested increased generation of succinate and fumarate respectively. Both metabolites play extensive roles in epigenetic reprogramming of macrophages, a characteristic also associated with macrophage training. Interestingly, increased expression of *Aoah* (encoding acyloxyacyl hydrolase), a gene usually upregulated on granulomas formed by mycobacteria (53) which may promote resolution of inflammation was also observed in BCG-vaccinated Isg15+ macrophages. ISGs associated with immune clearance were also upregulated including *Snx10* (phagosomal maturation), *Gtgn2* (M1 polarization) and *Itgal* (T cell recruitment) were upregulated following BCG vaccination and BCG-vaccinated, SCV2-challenged hamsters **(Fig. 5D)**. Lastly,

Isg15+ macrophages from BCG-vaccinated, SCV2 challenged animals also showed up-regulation of genes associated with attenuation of inflammatory responses such as *Socs3*, *Il18bp*, *Dusp1* and *Fos* as well as those which may counter tissue damage phenotype induced by inflammation such as *Il1rn* (regulator of IL-1α and IL-1β cytokines) and *Timp1* (tissue inhibitor of MMP1) **(Fig. 5D)**.

DEGs in Siglecf+ AMs. In unvaccinated, SCV2-infected animals Siglecf+ AMs highly expressed inflammatory genes (*Irf7*, *Irf9*, *Apobec1*, *Mx2*, *Mx1*, *Isg15*, *Ifit2*, *Rasd2*, *Herc6*, *Gbp5*, *Gbp7*, *Ifi44*, *Ifi47*, *Dhx58*, *Ifitm2*, *Igitp*, and *Cnp*) and genes involved in T cell recruitment and activation (*Ccl5*, *Ccrl2*, *Clec5a*, *Ltb*, *Ccl4CL4*, *Marcs1*, *Tnfsf10*, *Cd48*, *Alxox5*, *C3ar1*, *Cd80*, and *Cxcr2*). Genes characteristic of ER stress (*Gadd45*, *Gadd45b*, and *Atf4*) were also upregulated in *Siglecf*+ AMs of unvaccinated, SCV2-challenged animals **(Fig. 5E)**. In the Siglecf+ AMs of these same animals we also noted expression of genes are associated with signaling to plasmacytoid DCs and monocytic DCs (*Unc93b1*, *Lsp1*, *Slamf9* and *Batf*) suggesting a program to keep these key sentinel cells in and activated state. In contrast, in Siglecf+ AMs from BCG-vaccinated, SCV2-challenged hamster lungs we found upregulation of genes associated extracellular microbial sensing linked to NFκB signaling (*Cox1*, *Cox2*, *Cox3*, *Tnfsf13b*, *Hsp90ab1*, *Apoe1*, *Gtgn2* and *Ckap4P*). In addition, genes involved in phagocytosis (*Mrc1*), antigen presentation (*H2aa*), and suppression of inflammation (*Cdo1*, *Mertk, Mrc1*) were also upregulated in *Siglecf*+ AMs from BCG-vaccinated, SCV2-challenged hamsters **(Fig. 5E)**.

Non-immune cells are modulated by BCG vaccination. Since we did not enrich for immune cells prior to scRNAseq analysis, we were able to investigate non-immune cell responses. We were able to identify 5 types of non-immune cells (AT2, endothelial, ciliated, AT1, and fibroblasts) in hamster lungs. We identified both type I alveolar cells (AT1 cells), which are non-replicative,

362 thin flat squamous cells that form the basic structure of alveoli, as well as Type II cells (AT2 cells),
363 which are cuboidal, release pulmonary surfactant, and may differentiate into AT1 cells during lung
364 injury (54). Ciliated cells from bronchial epithelium, fibroblasts, and endothelial cells were also
365 present.
366
367 Consistent with ongoing inflammatory lung injury during SCV2 infection at D4 and D7, we found
368 that AT1, AT2, ciliated, and fibroblast cells were all significantly depleted in unvaccinated animals
369 (**Fig. 6A**). Interestingly, BCG vaccination prevented this depletion suggesting a global protective
370 effect by BCG against viral lung injury. Since this reversal of lung damage was most profound for
371 AT2 cells, we investigated the gene ontology of these cells in BCG-vaccinated animals and found
372 both an enhancement of genes involved in remodeling and response to injury as well as genes
373 involved in immune responses (**Fig. 6B**). In contrast, among non-vaccinated animals the gene
374 groups most strongly expressed in AT2 cells were those playing a role in viral responses and host
375 defenses (**Fig. 6C**).
376
377 AT2 cells possess immunomodulatory functions and are considered the immune cells of the
378 alveolar epithelium. Not surprisingly, when we evaluated DEGs in AT2 cells, we observed similar
379 patterns to those seen in lymphoid and myeloid cells. In the absence of vaccination, prominent
380 DEGs in AT2 cells were IFN-response genes (*Mx1*, *Mx2*, *Irf7*, *Irf9*, *Ifit2*, *Ifitm2*, *Slamf9*), antiviral
381 response genes (*Apobec1*, *Ifit2,* and *Ddx58)* (**Fig. 6D**). In contrast, in BCG-vaccinated hamsters,
382 AT2 DEGs were involved in immune clearance pathways such as antigen presentation (*H2-Ea*,
383 *H2-Oa*, *H2Aa*, *Ctss* [cathepsin S, lysosomal Ag processing]), the complement pathway (*C1qa*,
384 *C1qb C1qc*, *Cfd*), suppression of inflammation (*Ido1*), and lysosomal clearance (*Ubd*, *lipA*
385 [lysosomal acid lipase]).
386

Quantification of lung pathology using PET/CT. To evaluate pulmonary lung disease, SCV2 infected animals were imaged using ^{18}F-FDG PET/CT at the peak of lung disease (D4) after infection. The ^{18}F-FDG PET/CT analysis of lung consolidations did not reveal significant differences across the groups at D4 **(Fig. S7A-C)**.

Discussion

In this study we evaluated the impact of intravenous BCG vaccination on the pathogenesis and immunology of SCV2 lung infection in the golden Syrian hamster model using viral quantification, histology, and flow cytometry supplemented by scRNAseq analysis. The SCV2 virus levels, histology and flow results showed that BCG vaccination prevented SCV2 replication at the peak of infection (D4) and that it also reduced the development of bronchopneumonia both at D4 and D7. Concomitantly, BCG vaccination blunted T cell lymphopenia in the lungs and reduced granulocyte lung infiltration. BCG vaccination was also associated with a significant recruitment of macrophages to the lung.

Our study is the first to use single cell transcriptional analysis in BCG-vaccinated, SCV2 infected animals. Our scRNAseq data revealed that BCG vaccination 4 weeks prior to SCV2 challenge was associated with significant shifts both in the populations of cell types present in the lungs and in the DEGs expressed by these cell types. Among lymphoid cells, we noted a unique lung recruitment of plasma cells in BCG vaccinated animals that was absent in SCV2-infected animals and also in BCG vaccinated animals that were not SCV2 infected. These plasma cells showed higher gene signature scores associated with elevated immunoglobulin production suggesting that they are involved in a BCG-mediated acceleration of antibody production against the SCV2. This expansion of plasma cells and humoral response may in part be an anamnestic reaction, since peptide epitopes from BCG proteins and SARS-CoV-2 NSP3 and NSP13 proteins have shown to share significant homology and this may allow for potential cross-reactive adaptive

413 immunity (55,56). Several categories of CD4 T cells (Th1, Th17, Treg, and Tmem cells) as well
414 as CTLs were more abundant in the lungs of BCG vaccinated animals, and BCG-vaccination led
415 to reduced exhaustion scores in the gene expression profiles of some of these T cells. Th1 and
416 Tregs cells in the lung expressed high levels of type I IFN-associated genes in SCV2-infected
417 animals as would be expected with viral infection; however, in these same cell types, among
418 BCG-vaccinated, SCV2-infected lungs the predominant DEGs were shifted towards antigen
419 presentation.
420
421 Among macrophages, scRNAseq revealed that BCG vaccination alone recruits high levels AMs
422 to the lungs, a cell type associated with low inflammatory potential and clearance of pathogens.
423 Upon SCV2 infection, BCG-vaccinated animals retained these high levels of AMs, while they
424 dropped to low levels in SCV2-challenged, unvaccinated hamsters. In contrast we identified
425 several populations of interstitial macrophages that were considerably more abundant in lungs of
426 unvaccinated animals than in those that were BCG-vaccinated. As IM are non-resident
427 macrophages likely recruited from the periphery which are known to have high inflammatory
428 capacity, it is possible that a salutary immunologic effect of BCG is prevention of excess pro-
429 inflammatory IM recruitment. While the DEGs of both the AM and IM populations in unvaccinated
430 animals showed high expression of IFN-associated and chemokine genes, BCG vaccinated lungs
431 showed AM and IM that strongly expressed metabolic and repair genes.
432
433 This study is the first to show that intravenous BCG protects against SCV2 infection in hamsters.
434 We found a significant reduction of the SCV2 viral titer in BCG vaccinated animals at the peak of
435 infection on day 4. A recent study of both intravenous and subcutaneous BCG in two species of
436 hamsters (golden Syrian and Roborovski) found that neither route of vaccination protected either
437 hamster species against SCV2 challenge (30). Our study differed from that of Kaufmann et al. in
438 that we used a higher dose of BCG ($5x10^6$ as opposed to $1x10^6$ CFU), a higher viral challenge

dose ($5x10^5$ as opposed to $1x10^5$ or $1.4x10^4$ PFU), and our peak disease sacrifice time was one day later (day 4) than theirs (day 3). Two mouse-based studies have evaluated BCG vaccination for SCV2 using either a mouse-adapted SCV2 virus or the K18-hACE2 mouse model. The first found no protection with subcutaneous BCG (28), while the second found that intravenous BCG but not subcutaneous BCG was protective (29). Despite being a well-defined animal model of COVID-19 with human-like pathology, one key limitation of using golden Syrian hamsters is the limited immunological resources such as well-characterized and validated antibodies (anti-CD8 Abs for example) and the relative paucity of immunologic data on hamster immune responses for correlation with our scRNAseq data. Along these lines, it was surprising that no $CD8^+$ T cells were observed across the hamster groups even though they have been well-described in human scRNAseq studies of BAL samples in SCV2 (57,58).

While BCG vaccination is routinely used in most countries as a TB prevention, the vaccine is generally given intradermally, and recent human studies showing protection by BCG against COVID-19 disease also used intradermal BCG (13). Like other animal studies using BCG in animal models of SCV2 (28) we used the intravenous route based on literature that IV BCG is far more potent against tuberculosis in non-human primates , and evidence that IV BCG reprograms bone marrow hematopoietic stem cells towards a more protective state against bacterial challenge (22). Nevertheless, SCV2 animal studies using percutaneous BCG have shown significant immunologic benefits at the level of flow cytometry (29), and we anticipate that many of the scRNAseq shifts which we observed in IV BCG vaccinated hamsters would be present following intradermal BCG albeit potentially at a lower level.

In summary, our study reveals that BCG vaccination reduces SCV2 replication and prevents bronchopneumonia in hamsters by mechanisms that involve enhanced numbers of lung alveolar macrophages, blunting of SCV2-mediated T cell lymphopenia, and reduced lung granulocyte

infiltration. BCG appears to accelerate the appearance of immunoglobulin-producing plasma cells in the lung suggesting accelerated antiviral antibody production. The fact that BCG elevates the abundance of lung Treg cells while shifting a number of cell types away from expression of IFN-associated genes, suggests that BCG has immunotolerizing activity. These observations indicate that BCG vaccination may play a valuable role in protection against SCV2 and suggest that further studies of combining BCG with existing COVID-19 vaccines may offer synergistic protection.

Methods:

Study approval: All experiments with infectious SCV2 were carried out in Institutional Biosafety Committee approved BSL3 and ABSL3 facilities at The Johns Hopkins University School of Medicine using recommended positive pressure air respirators and protective equipment. Experimental procedure involving live animals were carried out in agreement with the protocol (#HA20M310) approved by the Institutional Animal Care and Use Committee (IACUC) at The Johns Hopkins University School of Medicine.

Bacterial strain and culture conditions: In this study we used commercially available *Mycobacterium bovis* (*M. bovis*) *Bacillus Calmette- Guérin* (BCG)-Tice (Onco-Tice©, Merck) for immunization experiments. The lyophilized bacterial stock was resuspended in 1ml of 7H9 Middlebrook liquid medium (Cat. B271310, Fisher Scientific) supplemented with (OADC) (Cat. B11886, Fisher Scientific), 0.5% glycerol (Cat. G55116, Sigma) and 0.05% Tween-80 (Cat. BP338, Fisher Scientific). The culture was streaked on 7H11 plate supplemented with oleic-albumin-dextrose-catalase (OADC) and single colonies were picked and propagated in 7H9 Middlebrook liquid medium for preparation of seed-stock. Individual seed-stock vial was randomly picked from frozen stock and was subsequently propagated in 7H9 medium before immunization.

Cells and viruses: All cells were obtained from the American Type Culture Collection (ATCC, Manassas, VA, USA). Vero C1008 [Vero 76, clone E6, Vero E6] (ATCC CRL-1586) cells were used for viral growth and determination of virus stock titers. Vero E6 cells were grown in MEM with 10% fetal bovine serum (FBS), L-glutamine, and penicillin-streptomycin at 37°C with 5% CO_2. SARS-CoV-2/Wuhan-1/2020 virus (U.S. Center for Disease Control and Prevention) was provided by Dr. Andrew Pekosz. The viral stocks were stored at -80°C and titers were determined by tissue culture infectious dose 50 ($TCID_{50}$) assay.

Animals: In vivo experiments involving BCG vaccination and SCV2 infection were carried out using male golden Syrian hamsters (*Mesocricetus auratus*). Male golden Syrian hamsters (age 5 to 6 weeks) were purchased from Envigo (Haslett, MI). Animals were housed individually under standard housing conditions (68 to 76°F, 30 to 70% relative humidity, 12-h light/12-h dark cycle) in cages with proper bedding (Teklad 7099 TEK-Fresh, Envigo, Indianapolis, IN) in the Animal Biosafety Level 3 (ABSL3) facility at Koch Cancer Research Building 2 (CRB2) at School of Medicine at The Johns Hopkins University. Animals were given ad libitum reverse osmosis (RO) water and feed (2018 SX Teklad, Envigo, Madison, WI). After 7 days of acclimatization animals were intravenously vaccinated using live 5 x 10^6 C.F.U. of BCG-Tice in a total volume of 100 ul saline under ketamine (60 to 80 mg/kg) and xylazine (4 to 5 mg/kg) anesthesia administered intraperitoneally. Control animals received an equivalent volume of saline. Animals were challenged using 5 x 10^5 $TCID_{50}$ of SCV2/Wuhan-1/2020 virus in 100 μl of DMEM (50 μl/naris) through the intranasal route under ketamine (60 to 80 mg/kg) and xylazine (4 to 5 mg/kg) anesthesia administered intraperitoneally. Control animals received an equivalent amount of DMEM. Animals were randomly assigned to be euthanized by isoflurane overdose at end points (day 4 and day 7) following SCV2 infection.

Experimental design: Groups of hamsters were intravenously (I.V.) administered saline or were vaccinated (I.V.) with 5x10^6 CFU of BCG-Tice. 30 days after vaccination animals were challenged with 5x10^5 $TCID_{50}$ units of SARS-CoV-2 (SCV2) (Wuhan-1/2020) by the intranasal route. At D4 and D7 post-challenge animals were sacrificed for analysis. 3 animals (BCG only) were not infected with SCV2 and were sacrificed 30 days post-vaccination to serve as controls (**Fig. 1A**).

Flow Cytometry analysis: For cellular immune profiling cell surface staining was performed on single cells from hamster lung and spleen tissues at the experimental end point. Briefly, tissues

were harvested and stored in sterile PBS in individual tubes before single cell preparations. Lung was extensively perfused using sterile PBS. We used mouse lung (Miltenyi Biotec; 130-095-927) and spleen dissociation kits (Miltenyi Biotec; 130-095-926) for preparation of single cells as per manufacturer's instruction using a gentleMACS™ Octo Dissociator with heaters (Miltenyi Biotec; 130-096-427). Cells were passed through a 70 μm filter and washed twice using ice-cold PBS followed by RBC lysis using ACK lysis buffer (Thermo Fisher Scientific: A1049201) at room temperature for 5 minutes. The cell viability was determined using Trypan blue dye staining and determine total live cells per lobe. For surface staining a total of 5 million cells per animal lung were used in this study. Briefly, cells were washed again using ice-cold PBS and stained using Zombie Aqua™ Fixable Viability Kit (Biolegend; 423101) for 20 min at room temperature. Cells were subsequently washed and resuspended in FACS buffer (1% BSA, 2mM EDTA in PBS) and incubated for 30 minutes at 4 °C in block buffer consisting of PBS and 2% FBS, 2% normal rat serum (Sigma Aldrich) and 2% normal mouse serum (Sigma Aldrich) prior to surface staining. Cells were again washed and stained with conjugated primary antibodies as per manufacturer's protocol. Following antibodies were used for cell surface staining: anti-CD3 (Bio-Rad, #MCA1477PB, CD3-12), anti-CD4 (BioLegend, #100451, GK1.5), anti-CD11b (Novus, #NB110-89474PECY7, Poly), and anti-RT1D (BioLegend, #110211, 14-4-4S). Cells were subsequently fixed using IC fixation buffer (eBiosciences™; 00-8222-49) for 60 minutes at 4 °C. Cells were washed three times using FACS buffer and acquired using BD LSRII with FACSDiva Software. Data analyses was carried out using FlowJo (v10) (TreesStar).

Sample and Preparation for scRNAseq: For single-cell RNA seq (scRNA-seq) of lung tissue derived single cells, whole right lung superior lobe was isolated from each animal. For single cell preparation, mouse lung dissociation kit (Miltenyi Biotec) was used with some additional modifications. Following single cell preparation, cell suspensions were applied to a MACS Smart Strainer (70 μm) and washed twice with 10 ml of DMEM. Cells were pelleted by spinning at 300

549 x g for a total of 7 minutes at 4°C. Cells were resuspended in 1ml DMEM containing 200 μl DNase
550 (1μg/μl) for 5 minutes at room temperature. Cells were washed by adding 10 ml sterile PBS
551 containing 0.5% BSA and pelleted at 4°C. The RBC lysis was carried out using 1X RBC lysis
552 solution (Miltenyi Biotec; 130-094-183) in a total volume of 1ml for 10 minutes at 4°C. Cells were
553 resuspended in 10 ml chilled DPBS containing 0.5% BSA and pelleted subsequently. Cells were
554 filtered using 35 μm Falcon cell strainer and transferred to a 2 ml lo-binding tube in a total volume
555 of 1ml DPBS containing 0.04% BSA. Cells were subsequently counted using trypan blue dye
556 exclusion assay to determine cell viability and total cell number.

557 **Single-cell RNA sequencing and data pre-processing**: Cells and gel beads were partitioned
558 using the 10X Genomics Chromium platform aiming for recovery of 10,000 cells per sample using
559 the Chromium Next GEM Single Cell 3' Reagent Kits v3.1 (Dual Index) (CG000315). After RNA
560 capturing, cDNA synthesis and library construction, the 3'DGE libraries were sequenced on
561 NovaSeq 6000 instrument to achieve a target sequencing depth of ~ 50,000 reads per cell.

562 Cell Ranger v4.0.0 was used to demultiplex the FASTQ reads and align them to the hamster
563 transcriptome. The resulting gene expression matrix were then loaded into Seurat (v4.0.4) (59) in
564 R (v4.0.3). ND1, ND2, ND4, ND5, ND6 were used to determine the percentage of mitochondrial
565 genes. The quality of cells was assessed based on the number of genes detected per cell and
566 the proportion of mitochondrial gene counts. Low-quality cells were filtered out if the number of
567 detected genes were below 500 or above 5,000. Cells were filtered out if the proportion of
568 mitochondrial gene counts was higher than 10%. In addition, genes that were expressed in less
569 than 5 cells were excluded.

570 **Data integration and cell type identification:** To compare cell types and proportions across
571 different groups, we applied the integration methods using the SCTransform workflow, which can
572 be used to assemble multiple distinct datasets into an integrated one and eliminate potential batch

effect (60). Briefly, top 3000 highly variable features were identified and used to find anchors between each dataset with FindIntegrationAnchors function of Seurat. Then these anchors were used to integrate different datasets together with IntegrateData function to create a batch-corrected data assay for downstream analysis.

Principal component analysis (PCA) was performed on the integrated data for dimensionality reduction and top 30 significant PCs were used for cluster analysis. After using FindNeighbors and FindClusters functions, we performed nonlinear dimensional reduction with the RunUMAP function to obtain a two-dimensional representation of the cells. Cells with similar transcriptome were clustered together. The FindAllMarkers function in Seurat was used to find marker genes of each cluster for cell type identification. Clusters were then annotated based on the expression of canonical cell marker genes described in previous study (61) and a single cell sequencing database PanglaoDB (https://panglaodb.se/) (62). Basically, *Arg1*, *Ccr2* and *Ccr5* for MDSCs , *Camp* and *Mmp9* for granulocyte, *Siglecf*, *Marco* and *Mrc1* for alveolar macrophage (AM), *C1qb* for interstitial macrophages (IMs), *Cd3d* and *Cd4* for T cell, *Sftpb* and *Sftpc* for alveolar epithelial cell, *Nkg7* and *Klrd1* for NK cell, *Mki67* for proliferating cell, *Ms4a1* and *Cd79b* for B cell, *Cfap44* and *Foxj1* for ciliated cell, *Vcam1* and *Vwf* for endothelial cell, *Irf8* and *Tcf4* for dendritic cells (DCs), *Jchain* and *Mzb1* for plasma cell, *Dcn* and *Col1a1* for fibroblast. Clusters expressing two or more canonical marker genes characteristic of different cell types, were classified as doublets and excluded from further analysis. Lymphoid, myeloid, and non-immune cell subpopulations were further sub-setted and extracted, and separately analyzed by dimensionality reduction with PCA and UMAP.

To compare the abundance of each cell types across different samples, cell type proportion was calculated as the number of cells within each cell cluster divided by the total number of cells of that sample.

Differentially expresses genes (DEGs) and pathway analysis: The FindMarker function in Seurat package was performed to identify differentially expressed genes between BCG-WT + SCV2 and SCV2 groups in a particular cell cluster. Benjamini–Hochberg method was used to adjust p-values for multiple tests. Genes expressed in at least 25% of cells in a cluster with adjusted P values < 0.05 were considered as differentially expressed genes. The gene filtering parameters used to generate each heatmap from differential gene expression analysis were described in each figure legend. GO term enrichment analysis of the DEGs was performed using Metascape (www.metascape.org) (63).

UCell analysis: UCell (64) is an R package, based on the Mann-Whitney U statistic, for calculating gene signatures in single-cell datasets . We used UCell score to evaluate the degree to which individual cells expressed a certain gene set. HALLMARK_INTERFERON_ALPHA_RESPONSE from MsigDB, Immunoglobulin production involved in immunoglobulin-mediated immune response (GO:0002381) and 6 well-defined exhaustion associated genes (*Lag3*, *Tigit*, *Pdcd1*, *Ctla4*, *Havcr2* and *Tox*) (65) were used as gene signature input to calculate UCell scores for each individual cell. UCell score violin plots were grouped by different samples and cell types.

Publicly available healthy control data: We additionally processed scRNA-seq data on hamster lung tissues by Nouailles et al. (61). Three datasets of lung samples from healthy hamsters (GSM4946629, GSM4946630, GSM4946631) were downloaded from the GEO database under accession code GSE162208. We processed the data using the similar strategy described above to filter low quality cells. Then MapQuery function in Seurat (v4.0.4) was performed to identify cell types using our own data reference. In brief, we transferred cell type labels from our reference data. Second, we integrated reference with query by correcting the low-dimensional embeddings.

620 Finally, we projected the query data onto the UMAP structure of the reference, which allowed us
621 to compare the abundance of the same cell type between datasets.

622 **Data availability:** Our single cell sequencing data publicly available at NCBI through the GEO
623 Series accession number GSE XXX [to be provided prior to publication]. The publicly available
624 datasets that we used in this study are available from GEO GSE162208 (61).
625
626 **Histochemistry and Immunohistochemistry.** Formalin-fixed paraffin embedded lung sections
627 were stained with hematoxylin-eosin (H&E) for analysis. Lung tissue was scored using a panel
628 of specific lung inflammation parameters according to criteria previous published on animal
629 models of acute pneumonia (66). All examinations were performed by a board-certified pulmonary
630 pathologist. Immunohistochemistry was performed on FFPE lung tissue sections for CD3 using
631 an automated Ventana Discovery (Roche, Basel, Switzerland) autostainer. Heat induced antigen
632 retrieval was achieved using ETDA pH9 solution (CC1, Roche). Primary antibody for CD3 (1:200
633 dilution; Cat# RM-9107-S1, Thermo Fisher Scientific) was incubated for 30m at 4 °C and detection
634 was achieved using UltraView DAB detection kit (Roche). Protein expression was scored by a
635 board-certified pulmonary pathologist blinded to cohort status or treatment group. CD3
636 membranous staining was evaluated separately in perivascular or peribronchial inflammation,
637 bronchial epithelium, alveolar wall as well as pneumocytes and in areas of pneumonia (when
638 present) or alveolar spaces (in absence of pneumonia). CD3 staining was scored as 1+ (scattered
639 single cells), 2+ (cells in clusters or sheets with at least 2 layers) or 3+ (several clusters or sheets).
640 Scores were then quantified using a point system (focal 1+= 0.5, 1+=1, focal 2+=1.5, 2+=2, 3+=3)
641 and total points were analyzed between treatment groups. Total CD3 expression was calculated
642 by combining all point scores for all criteria. Statistical analysis was performed between groups
643 at each timepoint (day 4 post infection and day 7 post infection) using Welch's t-test.
644

SCV2 viral quantification:

Quantification of SARS-CoV-2 infectious viral load in lung tissues

Following perfusion with phosphate-buffered saline (PBS), lung sections were collected, weighed and snap frozen on dry ice. Ice-cold virus titer buffer (Dulbecco's Modified Eagle Medium, 2% fetal bovine serum, 2 mM L-glutamine, 200 U/mL penicillin and 200 µg/mL streptomycin, 100 µg/mL gentamicin, 0.5 µg/mL amphotericin B) was added to the frozen lung samples at a 10% weight to volume ratio. The tissue was homogenized with ceramic 1.4 mm beads for 2 cycles of 20 seconds at a speed setting of 5000 rpm using a Precelley's Evolution homogenizer. Samples were centrifuged at 10,000 xg for 1 minute at 4°C to pellet the beads and tissue debris. In brief, lung homogenates were serially diluted in seven-point half-log dilutions and incubated on Vero C1008 cells in six technical replicates. Each sample was measured in triplicate. Plates were scored for CPE five days post infection using the CellTiter-Glo® Luminescent Cell Viability Assay per the manufacture's protocol (Promega). $TCID_{50}$ was calculated using the Reed and Muench method (67).

RNA extraction and RT-qPCR

Total RNA from hamster lung homogenates were extracted using TRIzol Reagent (Invitrogen) followed by the RNeasy kit (Qiagen) according to the manufacturer's protocol. cDNA was synthesized from total RNA using qScript cDNA SuperMix containing random hexamers and oligo-dT primers (Quanta Biosciences) following the manufacturer's protocol. Real-time PCR was performed in triplicate using TaqMan Fast Advanced Master Mix (Applied Biosystems) on a StepOnePlus Real Time PCR system (Applied Biosystems). SARS-CoV-2 RNA was detected using premixed forward (5'-TTACAAACATTGGCCGCAAA-3') and reverse (5'-GCGCGACATTCCGAAGAA-3') primers and probe (5'-FAM-ACAATTTGCCCCCAGCGCTTCAG-BHQ1-3') designed by the CDC as part of the 2019-nCoV CDC Research Use Only (RUO) kit (Integrated DNA Technologies, Catalog #10006713) to

671 amplify a region of the SARS-CoV-2 (SCV2) nucleocapsid (N) gene. PCR conditions were as
672 follows: 50°C for 2 min, 95°C for 2 min, followed by 45 cycles of 95°C for 3 s and 55°C for 30 s.
673 Serially diluted (10-fold) plasmid containing the complete SARS-CoV-2 N gene (Integrated DNA
674 Technologies, Catalog #10006625) was measured to generate a standard curve for quantification
675 of viral RNA copies. The limit of detection for the assay was 1 x 10^2 RNA copies. Viral copies
676 were normalized to the human RNase P (RP) gene using premixed forward (5'-
677 AGATTTGGACCTGCGAGCG-3') and reverse (5'-GAGCGGCTGTCTCCACAAGT-3') primers
678 and probe (5'-FAM-TTCTGACCTGAAGGCTCTGCGCG-BHQ-1-3') included in the same 2019-
679 nCoV CDC RUO kit.
680
681 **CT and PET imaging**: Four days post infection, live SCV2-infected male hamsters (n= 5 SCV2
682 and n= 6 BCG + SCV2) underwent chest CT using the nanoScan positron emission tomography
683 (PET)/CT (Mediso USA, MA, USA) small animal imager. Prior to PET imaging, hamsters were
684 administered ~10.22 MBq of ^{18}F-FDG (SOFIE, Sterling VA, USA) via the surgically implanted
685 center venous catheter. Given that SCV2 is designated as a BSL-3 pathogen, live SCV2-infected
686 animals were imaged inside transparent and sealed biocontainment cells developed in-house,
687 compliant with BSL-3 containment and capable of delivering air-anesthetic mixture to sustain live
688 animals during imaging (68,69). A 15-min PET acquisition and subsequent CT were performed
689 using the nanoScan PET/CT (Mediso Alrington, VA). CT images were visualized and analyzed
690 using the VivoQuant 2020 lung segmentation tool (Invicro, MA, USA) (69). Briefly, an entire lung
691 volume (LV) was created, and volumes of interests (VOIs) were shaped around the pulmonary
692 lesions using global thresholding for Hounsfield Units (HU) ≥ 0, and disease severity (CT score)
693 was quantified as the percentage of diseased lung in each animal. The investigators were blinded
694 to the group assignments. The data are represented as CT score [(pulmonary lesions
695 volume/whole lung volume) × 100]. The investigators analyzing the CT were blinded to the group
696 assignments. VivoQuant™ 2020 (Invicro, Boston, MA, USA) was used for visualization and

quantification. Scatter and attenuation corrections were applied to the PET data and multiple VOIs were manually drawn per animal using the CT as a reference.

Author contributions

A.K.S., R.W, W.R.B., S.Y., and T.J.B co-led the study through conceptualization, design, oversight, and interpretation of results. W.R.B. obtained the funding for the study. A.K.S. designed, conducted, and interpreted the results of the experiments. A.K.S., R.W., K.A.L., M.P. C.K.B, P.U., A.A.O., S.D., O.K., M. B., P.I., and K.J.P. conducted then experiments and provided key experts advice. S.K.J., and T.J.B. assisted in the design of the experiments and provided key expert advice. A.K.S., and W.R.B wrote the manuscript. A.K.S., R.W. K.A.L., M.P., C.K.B., O.K., A.A.O., K.J.P., S.K.J., T.J.B., S.Y and W.R.B. revised and edited the manuscript. A.K.S., and W.R.B. designed and produced figures for this manuscript.

712 **Supplemental material**

713

714 **Table S1: Table showing cell counts each in different immune and non-immune subsets**

Cell counts for single cell RNA sequencing (scRNAseq)					
Animal	**Lymphoid**	**Myeloid**	**Non-immune**	**Cells used for analysis**	**Average Cell/animal**
BCG					
BCG-1	229	8417	279	8925	**11249**
BCG-2	1602	10706	1768	14076	
BCG-3	1285	7931	1530	10746	
Total				**33747**	
SARS-CoV-2					
SCV2 (D4)-1	372	7606	249	8227	**8643.75**
SCV2 (D4)-2	447	7365	270	8082	
SCV2 (D7)-1	1525	8264	324	10113	
SCV2 (D7)-2	173	7807	173	8153	
Total				**34575**	
BCG + SCV2					
BCG+ SCV2 (D4)-1	703	7367	410	8480	**7434.33**
BCG+ SCV2 (D4)-2	896	6759	485	8140	
BCG+ SCV2 (D4)-3	1020	6880	319	8219	
BCG+ SCV2 (D7)-1	1003	6290	785	8078	
BCG+ SCV2 (D7)-2	1832	5828	402	8062	
BCG+ SCV2 (D7)-3	301	2969	357	3627	
Total				**44606**	

715 **Table S2: Table showing identified cell types in this study based on specific marker**

716 **genes**

Identification of different cell types based on marker genes		
No.	**Cell Type**	**Marker Genes**
Immune cells (Myeloid)		
1	Granulocyte	*Mmp9*, *Camp*
2	G-MDSC	*Cd14*, *Arg1*
3	Marco+AM	*Marco*, *Mrc1*
4	IM	*C1qa*, *C1qb*
5	M-MDSC	*Ccr2*, *Ccr5*
6	Siglecf+AM	*Siglecf*
7	Dendritic Cells	*Tcf4*
8	Proliferating macrophages	*Macrco, Mki67*
Immune cells (Lymphoid)		
8	T cells	*Cd3d*, *Cd4*
9	NK	*Nkg7*, *Prf1*
10	B cells	*Cd79b*, *Ms4a1*
11	Plasma cells	*Jchain*, *Mzb1*
Non-immune cells		
12	Alveolar epithelial	*Sftpb*, *Sftpc*
13	Ciliated	*Foxj1*, *Cfap44*
14	Endothelial	*Vcam1*, *Vwf*
15	Fibroblast	*Dcn*, *Col1a1*
17	Proliferating cells	*Mki67*, *Top2a*

Acknowledgements

The generous support of grants AI155346 from the NIH and grant #2167 from Emergent Ventures at the Mercatus Center, George Mason University is gratefully acknowledged. This study was also supported by NIH grant U54CA260492 (providing support to S.Y. and R.W.). We thank the members of the Sidney Kimmel Comprehensive Cancer Center's Experimental and Computational Genomics Core, supported by NIH Grant P30CA006973, for their support of the next generation sequencing experiments. The authors also thank Geetha Srikrishna, Ada Tam and Lee Blosser for technical assistance.

Conflicts of interest: The authors have declared that no conflict of interest exists.

730 **Figure Legends:**

731

732 **Main Figures:**

733 **Figure 1. BCG vaccination diminishes SARS-CoV-2 (SCV2) infection induced lung**
734 **inflammation and viral load in golden Syrian hamsters. A.** Experimental layout. **B-C.**
735 Bronchopneumonia at day 4 (D4) and day 7 (D7) after SARS-CoV-2 infection, mild local
736 inflammation (arrows) in BCG + SCV2 lungs. Neutrophils **(D)** and macrophage **(E)** infiltration at
737 D4 after SARS-CoV-2 infection. **F.** $CD3^+$ lymphocyte positivity scores at D4 in hamster lungs after
738 SARS-CoV-2 infection. **G-H.** Bar graph showing SARS-CoV-2 viral load in the lung at D4 and D7
739 post infection in non-vaccinated and BCG-vaccinated hamsters. Briefly, Infective viral particles
740 **(G)** were quantified from a standard of infectious virus and expressed at $TCID_{50}$ equivalents per
741 mg lung tissues. Dotted lines indicate lower limit of detection (LOD). Viral RNA levels **(H)** were
742 determined in the lungs, normalized against human RNaseP and were transformed to estimate
743 viral RNA copies per 100 ng of total lung RNA. Data points represent number of animals used per
744 group. Statistical analysis was done using two-sided Fisher exact test **(C-E)**, Welch's t-test **(F)** or
745 two-tailed Student's t-test **(G-H)** (significant when $P < 0.05$). Percent animals and 95% confidence
746 intervals (CI) showing pathology were (**C**) bronchopneumonia in the BCG-SCV2 group at D4 0%
747 (95% CI: 0, 45.9%), at D7 28.6% (95% CI: 36.7, 71.0%); (**D**) neutrophil infiltration in the BCG-
748 SCV2 group at D4 50% (95% CI: 11.8, 88.2%); (**E**) macrophage infiltration in the BCG-SCV2
749 group 83.3% (95% CI: 35.9, 99.6%) and in the SCV2 only group at D4 60.0% (95% CI: 14.7,
750 94.7%). A schematic of CD3 positivity **(F)** is given in methods section.

751

752 **Figure 2. Differential abundance of lymphocytes, macrophages and granulocytes in BCG**
753 **vaccinated golden Syrian hamster lungs after SARS-CoV-2 infection.** Differential
754 percentages of **A.** $CD3^+$ lymphocytes. **B.** $CD4^+$ T cells within the lymphocyte compartment. **C.**
755 macrophages ($CD11b^{(lo)}$ $MHCII^{(hi)}$ of live cells) and, **D.** granulocytes ($CD11b^{(+ve)}$ $MHCII^{(-ve)}$ of live

cells) in the lung of hamsters. Single cells preparations from lung tissues following necropsy were investigated for different lymphoid and myeloid cells using multicolor flow-cytometry. The data are presented as mean values ± S.E.M. Statistical analyses were done using one-way ANOVA with the p-values indicated.

Figure 3. Cellular landscape of SARS-CoV-2 infected hamster lungs after BCG vaccination identified by scRNAseq. A. Uniform Manifold Approximation and Projection (UMAP) plot showing identification of 17 different major cell-type in hamster lungs integrated by all samples. **B.** UMAP plot showing lung cellular dynamics in hamster lungs in BCG vaccinated, SARS-CoV-2 (SCV2) infected, and BCG + SARS-CoV-2 (SCV2) infected animals at D4 after SCV2 infection. **C.** UCell score distribution in UMAP plot for cell type marker gene signatures (**listed in Table S2**) evaluated using UCell. **D.** Dot plots of log-normalized expression and fraction of cells expressing selected canonical marker genes for identification of 17 different cell types in hamster lungs across all samples.

Figure 4. BCG vaccination strongly affects lung lymphoid dynamics and gene activation programs in different lymphoid subsets in SARS-CoV-2 infected hamster lungs. A. Bar graph showing average proportion of different lymphocytic cells across groups. Violin plots showing UCell scores for **(B)** immunoglobulin production on plasma cells, and **(C)** exhaustion scores on Th1 cells across different groups. Horizontal lines represent mean values. All differences with $P < 0.01$ are indicated. **$P < 0.01$, ***$P < 0.001$, ****$P < 0.0001$ (one-way ANOVA). Th1 lymphocyte-linked gene ontology enrichment analysis of biological processes showing gene sets that enriched in **(D)** SARS-CoV-2 (SCV2) versus BCG + SARS-CoV-2 (SCV2), and in **(E)** BCG + SARS-CoV-2 (SCV2) versus SARS-CoV-2 (SCV2) across both time-points. A darker color indicates a smaller P value. **F.** Heat map depicting the average expression value of top differentially expressed genes (DEGs) across different treatment conditions in Th1 cells. Top

782 DEGs were selected with adjusted P-value < 0.05 and average fold change >0.7. Volcano plots
783 depicting DEGs in **(G)** Th1, **(H)** Th17, and **(I)** regulatory T cells (Tregs). The x-axis indicates
784 log_2FC of gene expression in BCG + SCV2 compared to SCV2 group.
785
786 **Figure 5. BCG vaccination curtails SCV2 mediated lung inflammation by modulating**
787 **myeloid cell abundance and phenotypes. A.** Bar diagram showing average proportion of
788 different myeloid cells across groups. **B.** Dot plot showing the expression levels of a group of
789 chemokines and cytokines in Isg15+ macrophages across different groups. **C.** Violin plots
790 showing UCell gene signature scores of hallmark type I IFN (Interferon-α) responses in 5 major
791 myeloid cells in hamster lungs across different groups. All differences with P < 0.01 are indicated.
792 **P < 0.01, ***P < 0.001, ****P < 0.0001 (one-way ANOVA). Heat map depicting the average
793 expression value of top differentially expressed genes (DEGs) across different groups in **(D)**
794 Isg15+ macrophages, and **(E)** Siglecf+ alveolar macrophages (AMs). Top DEGs were selected
795 with adjusted P-value < 0.05 and average fold change > 0.7.
796
797 **Figure 6. BCG vaccination restores AT2 cells and causes extensive phenotypic changes**
798 **in non-immune cells in SARS-CoV-2 (SCV2) infected hamster lungs. A.** Bar graph showing
799 average proportion of different lung non-immune cells across groups. AT2 cell-linked gene
800 ontology enrichment analysis of biological processes showing gene sets that enriched in **(B)** BCG
801 + SARS-CoV-2 (SCV2) versus SARS-CoV-2 (SCV2), and in **(C)** SARS-CoV-2 (SCV2) versus
802 BCG + SARS-CoV-2 (SCV2) across both time-points, and **D.** heat map depicting the average
803 expression values of top differentially expressed genes (DEGs) across different groups in AT2
804 cells. Top DEGs were selected with adjusted P-value < 0.05 and average fold change > 0.7.
805
806 **Supplementary Figures**
807

Supplementary Figure S1. Lymphocyte infiltration and granuloma formation in BCG vaccinated golden Syrian hamsters after SARS-CoV-2 infection. A. total $CD3^+$ lymphocytes at day 7 (D7). **B.** $CD3^+$ lymphocytes in perivascular area, and **C.** Granuloma formation and inflammation. Left panel showing HPF (200x) view of SARS-CoV-2 infected lungs showing alveolated parenchyma with marked pneumocyte atypia (arrowheads) acute inflammation (neutrophils showed by arrows) and breakdown of architecture sonsistent with acute lung injury secondary to pneumonia. Right panel HPF showing intraalveolar small non-necrotizing granuloma surrounded by abundant lymphocytes (arrowheads) and macrophages (arrows) in hamster lung at day 4 after SARS-CoV-2 challenge. Bar graph showing pathological quantification of granulomata after BCG vaccination. Data points represent number of animals per grouop. Data presented as mean values ± S.E.M. Statistical analyses done using Welch's t-test (P value < 0.05 considered significance). Schematic of CD3 positivity is given in methods section.

Supplementary Figure S2. Differential abundance of lymphocytes and myeloid cells in hamster spleens across different groups. Bar graph showing percentages of **A.** total lymphocytes ($CD3^+$). **B.** CD4+ T cells within lymphocytic compartment ($CD4^+$ of CD3). **C.** macrophages ($CD11b^+RT1D^+$ of $CD3^-$), and **D.** granulocytes ($CD11b^+RT1D^-$ of $CD3^-$) within non-lymphocytic compartment. Data points represent the number of animals assigned per group. Data are represented as mean values ± S.E.M. The statistical analyses were done using one-way ANOVA (P values <0.05 was considered significant).

Supplementary Figure S3. Heat map showing top 5 most upregulated genes across 17 cell types identified within immune (myeloid and lymphoid) and non-immune cells using single cell RNA sequencing (scRNAseq) analysis.

Supplementary Figure S4. Identification of different lymphocytic sub-set of cells across groups. A. Uniform Manifold Approximation and Projection (UMAP) plot showing 10 lymphocytic sub-sets using the cognate markers. **B.** UMAP plot showing dynamic changes in abundance of different lymphocytic cells across groups at both time points. **C.** Dot plot showing average expression of markers genes used to assign cellular identity, and **D.** Heat map showing top 5 genes expressed in different lymphoid subsets.

Supplementary Figure S5. BCG vaccination induced remodeling of myeloid cells in animal lungs after SARS-CoV-2 infection. A. Uniform Manifold Approximation and Projection (UMAP) plot showing different myeloid cells in hamster lungs after SCV2 infection (this study) and in healthy age-matched hamsters (without SCV2 infection, public database). Average proportion of **B.** Th1, Treg and plasma cells. **C.** Major myeloid subsets, and **D.** Alveolar epithelial cells in hamster lungs across different groups.

Supplementary Figure S6. Identification of different myeloid sub-sets of cells across all samples. A. Uniform Manifold Approximation and Projection (UMAP) plot showing different myeloid subset of cells integrated across all samples. **B.** Dot plot showing average expression and percentage cells expressing marker genes used to define different myeloid sub-sets.

Supplementary Figure S7. Monitoring lung pneumonia in hamsters infected with SARS-CoV-2 using ^{18}F-FDG PET/CT. (A) The affected lung areas were determined for each SARS-CoV-2-infected hamster using CT. Automated lung segmentation of the CT images was performed and data is represented as percentage of the lung determined to be affected based on tissue density. **(B)** ^{18}F-FDG PET/CT was performed in SARS-CoV-2-infected hamsters. The ^{18}F-FDG PET signal in affected lung areas, as determined by the automated lung segmentation, was quantified, and is represented as mean standardized uptake value (SUVmean). The data is

859 represented as median ± interquartile range. **(C)** Transverse ^{18}F-FDG PET/CT of representative
860 SARS-CoV-2-hamsters from the BCG-vaccinated and control groups. Increased ^{18}F-FDG PET
861 signal was observed in the areas of lung consolidation observed in CT (yellow arrows).
862

References

1. Brinkley-Rubinstein L, Peterson M, Martin R, Chan P, Berk J. Breakthrough SARS-CoV-2 Infections in Prison after Vaccination [Internet]. *N Engl J Med* 2021;385(11):1051–1052.

2. Harvey WT et al. SARS-CoV-2 variants, spike mutations and immune escape. *Nat Rev Microbiol* 2021;19(7):409–424.

3. Bar-On YM et al. Protection of BNT162b2 Vaccine Booster against Covid-19 in Israel. *N Engl J Med* 2021;385(15):1393–1400.

4. Cromer D et al. Neutralising antibody titres as predictors of protection against SARS-CoV-2 variants and the impact of boosting: a meta-analysis. *Lancet Microbe* 2022;3(1):e52–e61.

5. Chen L et al. Elevated serum levels of S100A8/A9 and HMGB1 at hospital admission are correlated with inferior clinical outcomes in COVID-19 patients. *Cell Mol Immunol* 2020;17(9):992–994.

6. Chen I-Y, Moriyama M, Chang M-F, Ichinohe T. Severe Acute Respiratory Syndrome Coronavirus Viroporin 3a Activates the NLRP3 Inflammasome. *Front Microbiol* 2019;10:50.

7. Tay MZ, Poh CM, Rénia L, MacAry PA, Ng LFP. The trinity of COVID-19: immunity, inflammation and intervention. *Nat Rev Immunol* 2020;20(6):363–374.

8. Lucas C et al. Longitudinal analyses reveal immunological misfiring in severe COVID-19. *Nature* 2020;584(7821):463–469.

9. Tian Y et al. Single-cell immunology of SARS-CoV-2 infection. *Nat Biotechnol* 2022;40(1):30–41.

885 10. Carvalho T, Krammer F, Iwasaki A. The first 12 months of COVID-19: a timeline of
886 immunological insights. *Nat Rev Immunol* 2021;21(4):245–256.

887 11. Giamarellos-Bourboulis EJ et al. Activate: Randomized Clinical Trial of BCG Vaccination
888 against Infection in the Elderly. *Cell* 2020;183(2):315-323.e9.

889 12. Netea MG, van der Meer JW, van Crevel R. BCG vaccination in health care providers and the
890 protection against COVID-19. *J Clin Invest* 2021;131(2):145545.

891 13. Tsilika M et al. ACTIVATE-2: a double-blind randomized trial of BCG vaccination against
892 COVID19 in individuals at risk.medRxiv 2021.05.20.21257520.
893 https://doi.org/10.1101/2021.05.20.21257520

894 14. Ma J et al. *Mycobacterium tuberculosis* multistage antigens confer comprehensive protection
895 against pre- and post-exposure infections by driving Th1-type T cell immunity. *Oncotarget*
896 2016;7(39):63804–63815.

897 15. Rahman MJ, Fernández C. Neonatal vaccination with *Mycobacterium bovis* BCG: potential
898 effects as a priming agent shown in a heterologous prime-boost immunization protocol. *Vaccine*
899 2009;27(30):4038–4046.

900 16. Wu Y et al. Heterologous Boost Following *Mycobacterium bovis* BCG Reduces the Late
901 Persistent, Rather Than the Early Stage of Intranasal Tuberculosis Challenge Infection. *Front*
902 *Immunol* 2018;9:2439.

903 17. Moorlag SJCFM, Arts RJW, van Crevel R, Netea MG. Non-specific effects of BCG vaccine on
904 viral infections. *Clin Microbiol Infect* 2019;25(12):1473–1478.

905 18. Singh AK, Netea MG, Bishai WR. BCG turns 100: its nontraditional uses against viruses,
906 cancer, and immunologic diseases. *J Clin Invest* 2021;131(11):148291.

907 19. Kleinnijenhuis J et al. Long-lasting effects of BCG vaccination on both heterologous Th1/Th17
908 responses and innate trained immunity. *J Innate Immun* 2014;6(2):152–158.

909 20. Chua W-J et al. Polyclonal mucosa-associated invariant T cells have unique innate functions
910 in bacterial infection. *Infect Immun* 2012;80(9):3256–3267.

911 21. Steigler P et al. BCG vaccination drives accumulation and effector function of innate lymphoid
912 cells in murine lungs [Internet]. *Immunol Cell Biol* 2018;96(4):379–389.

913 22. Kaufmann E et al. BCG Educates Hematopoietic Stem Cells to Generate Protective Innate
914 Immunity against Tuberculosis. *Cell* 2018;172(1–2):176-190.e19.

915 23. Arts RJW et al. BCG Vaccination Protects against Experimental Viral Infection in Humans
916 through the Induction of Cytokines Associated with Trained Immunity. *Cell Host Microbe*
917 2018;23(1):89-100.e5.

918 24. Leentjens J et al. BCG Vaccination Enhances the Immunogenicity of Subsequent Influenza
919 Vaccination in Healthy Volunteers: A Randomized, Placebo-Controlled Pilot Study. *J Infect Dis*
920 2015;212(12):1930–1938.

921 25. Salem A, Nofal A, Hosny D. Treatment of common and plane warts in children with topical
922 viable Bacillus Calmette-Guerin. *Pediatr Dermatol* 2013;30(1):60–63.

923 26. Lodmell DL, Ewalt LC. Enhanced resistance against encephalomyocarditis virus infection in
924 mice, induced by a nonviable *Mycobacterium tuberculosis* oil-droplet vaccine. *Infect Immun*
925 1978;19(1):225–230.

926 27. Kulkarni S et al. *Bacillus Calmette-Guérin* Confers Neuroprotection in a Murine Model of
927 Japanese Encephalitis. *Neuroimmunomodulation* 2016;23(5–6):278–286.

928 28. Counoupas C et al. A single dose, BCG-adjuvanted COVID-19 vaccine provides sterilizing
929 immunity against SARS-CoV-2 infection. *NPJ Vaccines* 2021;6(1):143.

930 29. Hilligan KL et al. Intravenous administration of BCG protects mice against lethal SARS-CoV-
931 2 challenge. *J Exp Med* 2022;219(2):e20211862.

932 30. Kaufmann E et al. BCG vaccination provides protection against IAV but not SARS-CoV-2. *Cell*
933 *Rep* 2022;110502.

934 31. Meyer M et al. Attenuated activation of pulmonary immune cells in mRNA-1273-vaccinated
935 hamsters after SARS-CoV-2 infection. *J Clin Invest* 2021;131(20):e148036.

936 32. Thompson EA et al. Metabolic programs define dysfunctional immune responses in severe
937 COVID-19 patients. *Cell Rep* 2021;34(11):108863.

938 33. Majdoul S, Compton AA. Lessons in self-defence: inhibition of virus entry by intrinsic immunity.
939 *Nat Rev Immunol* [published online ahead of print: October 13, 2021]; doi:10.1038/s41577-021-
940 00626-8

941 34. Farr L, Ghosh S, Moonah S. Role of MIF Cytokine/CD74 Receptor Pathway in Protecting
942 Against Injury and Promoting Repair. *Front Immunol* 2020;11:1273.

943 35. Hartmann C et al. The Pathogenesis of COVID-19 Myocardial Injury: An
944 Immunohistochemical Study of Postmortem Biopsies. *Front Immunol* 2021;12:748417.

945 36. Tomić S et al. Reduced Expression of Autophagy Markers and Expansion of Myeloid-Derived
946 Suppressor Cells Correlate With Poor T Cell Response in Severe COVID-19 Patients. *Front*
947 *Immunol* 2021;12:614599.

948 37. Hou H et al. Immunologic memory to SARS-CoV-2 in convalescent COVID-19 patients at 1
949 year post infection. *J Allergy Clin Immunol* 2021;148(6):1481-1492.e2.

950 38. Prelli Bozzo C et al. IFITM proteins promote SARS-CoV-2 infection and are targets for virus
951 inhibition in vitro. *Nat Commun* 2021;12(1):4584.

952 39. Gordon DE et al. A SARS-CoV-2 protein interaction map reveals targets for drug repurposing.
953 *Nature* 2020;583(7816):459–468.

954 40. Zhang Q et al. Inborn errors of type I IFN immunity in patients with life-threatening COVID-19.
955 *Science* 2020;370(6515):eabd4570.

956 41. Allard B, Panariti A, Martin JG. Alveolar Macrophages in the Resolution of Inflammation,
957 Tissue Repair, and Tolerance to Infection. *Front Immunol* 2018;9:1777.

958 42. Koeken VACM et al. The effect of BCG vaccination on alveolar macrophages obtained from
959 induced sputum from healthy volunteers. *Cytokine* 2020;133:155135.

960 43. Dewhurst JA et al. characterization of lung macrophage subpopulations in COPD patients and
961 controls. *Sci Rep* 2017;7(1):7143.

962 44. Upadhyay AA et al. TREM2+ and interstitial macrophages orchestrate airway inflammation in
963 SARS-CoV-2 infection in rhesus macaques. *bioRxiv* 2021;2021.10.05.463212.

964 45. Pérez-Gómez A et al. Dendritic cell deficiencies persist seven months after SARS-CoV-2
965 infection. *Cell Mol Immunol* 2021;18(9):2128–2139.

966 46. Hadjadj J et al. Impaired type I interferon activity and inflammatory responses in severe
967 COVID-19 patients. *Science* 2020;369(6504):718–724.

968 47. Arunachalam PS et al. Systems biological assessment of immunity to mild versus severe
969 COVID-19 infection in humans. *Science* 2020;369(6508):1210–1220.

970 48. Reizine F et al. SARS-CoV-2-Induced ARDS Associates with MDSC Expansion, Lymphocyte
971 Dysfunction, and Arginine Shortage. *J Clin Immunol* 2021;41(3):515–525.

972 49. Agrati C et al. Expansion of myeloid-derived suppressor cells in patients with severe
973 coronavirus disease (COVID-19). *Cell Death Differ* 2020;27(11):3196–3207.

974 50. Sacchi A et al. Early expansion of myeloid-derived suppressor cells inhibits SARS-CoV-2
975 specific T-cell response and may predict fatal COVID-19 outcome. *Cell Death Dis*
976 2020;11(10):921.

977 51. Takano T et al. Myeloid cell dynamics correlating with clinical outcomes of severe COVID-19
978 in Japan. *Int Immunol* 2021;33(4):241–247.

979 52. Arts RJW et al. Immunometabolic Pathways in BCG-Induced Trained Immunity. *Cell Rep*
980 2016;17(10):2562–2571.

981 53. Zou B et al. Acyloxyacyl hydrolase promotes the resolution of lipopolysaccharide-induced
982 acute lung injury. *PLoS Pathog* 2017;13(6):e1006436.

983 54. Olajuyin AM, Zhang X, Ji H-L. Alveolar type 2 progenitor cells for lung injury repair. *Cell Death*
984 *Discov* 2019;5:63.

985 55. Urbán S, Paragi G, Burián K, McLean GR, Virok DP. Identification of similar epitopes between
986 severe acute respiratory syndrome coronavirus-2 and *Bacillus Calmette-Guérin*: potential for
987 cross-reactive adaptive immunity. *Clin Transl Immunology* 2020;9(12):e1227.

988 56. Eggenhuizen PJ et al. BCG Vaccine Derived Peptides Induce SARS-CoV-2 T Cell Cross-
989 Reactivity. *Front Immunol* 2021;12:692729.

990 57. Ren X et al. COVID-19 immune features revealed by a large-scale single-cell transcriptome
991 atlas. *Cell* 2021;184(7):1895-1913.e19.

992 58. Xu G et al. The differential immune responses to COVID-19 in peripheral and lung revealed
993 by single-cell RNA sequencing. *Cell Discov* 2020;6:73.

994 59. Hao Y et al. Integrated analysis of multimodal single-cell data. *Cell* 2021;184(13):3573-
995 3587.e29.

996 60. Stuart T et al. Comprehensive Integration of Single-Cell Data. *Cell* 2019;177(7):1888-
997 1902.e21.

998 61. Nouailles G et al. Temporal omics analysis in Syrian hamsters unravel cellular effector
999 responses to moderate COVID-19. *Nat Commun* 2021;12(1):4869.

1000 62. Franzén O, Gan L-M, Björkegren JLM. PanglaoDB: a web server for exploration of mouse
1001 and human single-cell RNA sequencing data. *Database (Oxford)* 2019;2019:baz046.

1002 63. Zhou Y et al. Metascape provides a biologist-oriented resource for the analysis of systems-
1003 level datasets. *Nat Commun* 2019;10(1):1523.

1004 64. Andreatta M, Carmona SJ. UCell: Robust and scalable single-cell gene signature scoring.
1005 *Comput Struct Biotechnol J* 2021;19:3796–3798.

1006 65. Zhang J-Y et al. Single-cell landscape of immunological responses in patients with COVID-
1007 19. *Nat Immunol* 2020;21(9):1107–1118.

1008 66. Dietert K et al. Spectrum of pathogen- and model-specific histopathologies in mouse models
1009 of acute pneumonia. *PLoS One* 2017;12(11):e0188251.

1010 67. Lindenbach BD. Measuring HCV infectivity produced in cell culture and in vivo. *Methods Mol*
1011 *Biol* 2009;510:329–336.

1012 68. Dhakal S et al. Sex differences in lung imaging and SARS-CoV-2 antibody responses in a
1013 COVID-19 golden Syrian hamster model. *bioRxiv* 2021;2021.04.02.438292.

1014 69. Ruiz-Bedoya CA et al. 124I-Iodo-DPA-713 Positron Emission Tomography in a Hamster
1015 Model of SARS-CoV-2 Infection. *Mol Imaging Biol* 2022;24(1):135–143.

1016

1017

Figure 1

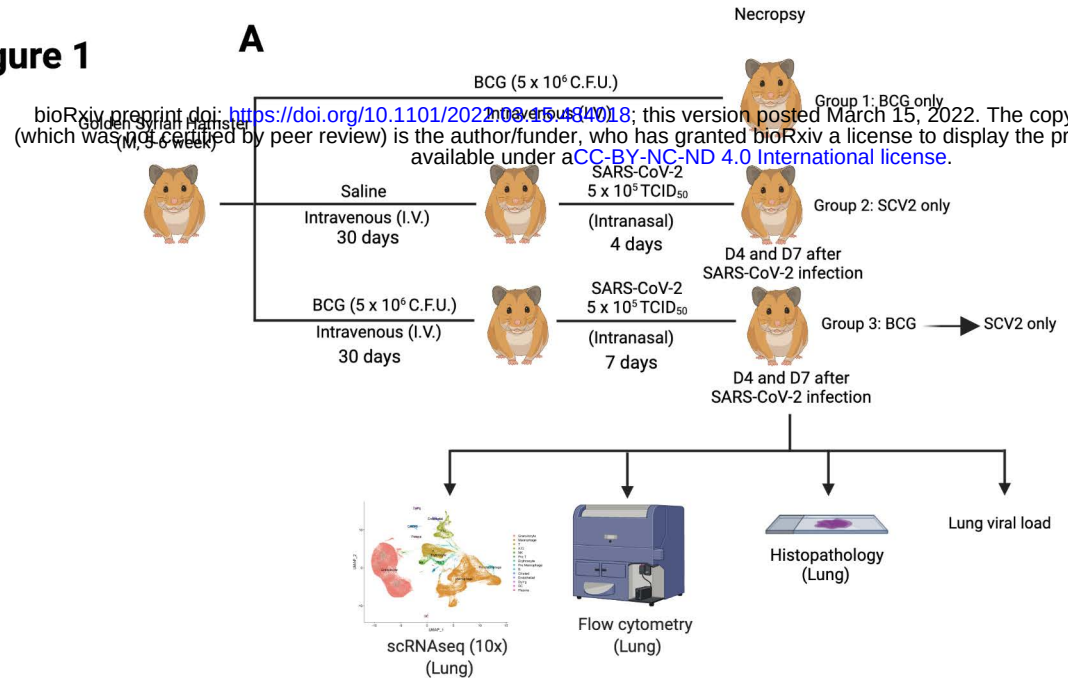

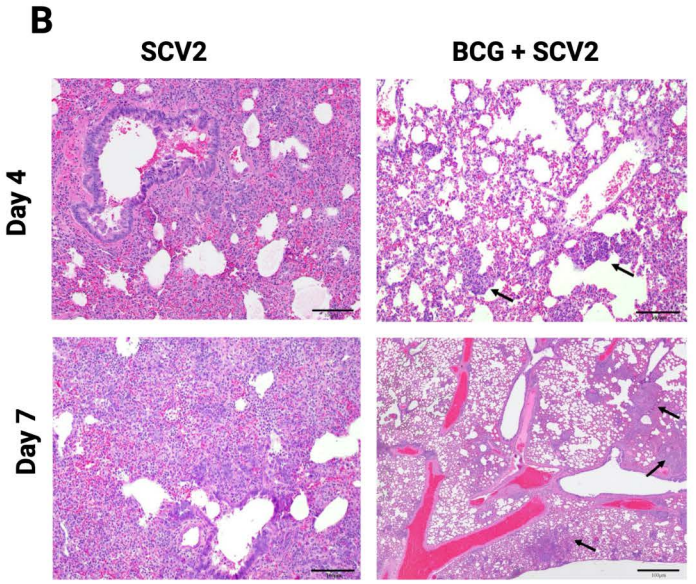

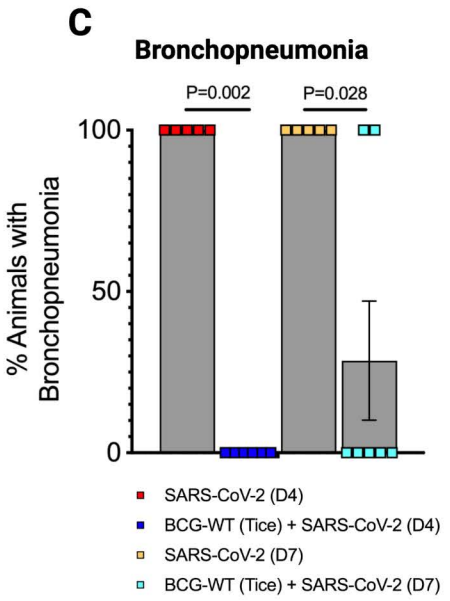

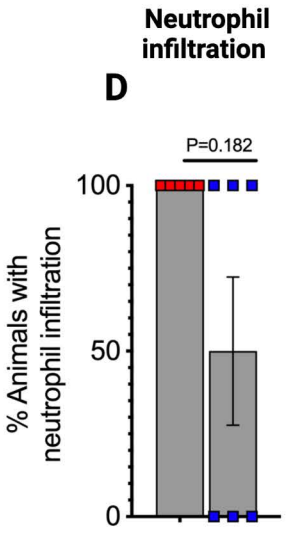

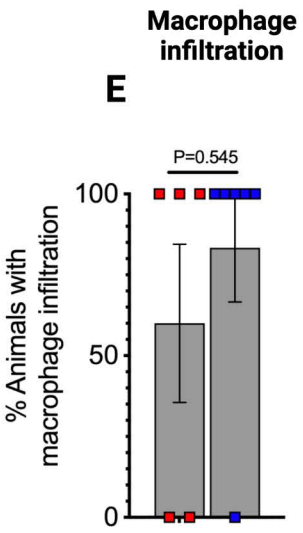

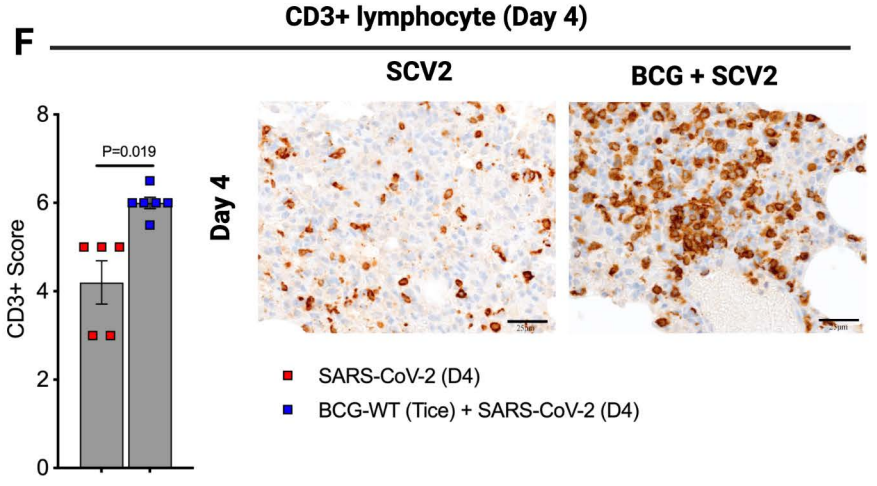

Figure 1. Continued

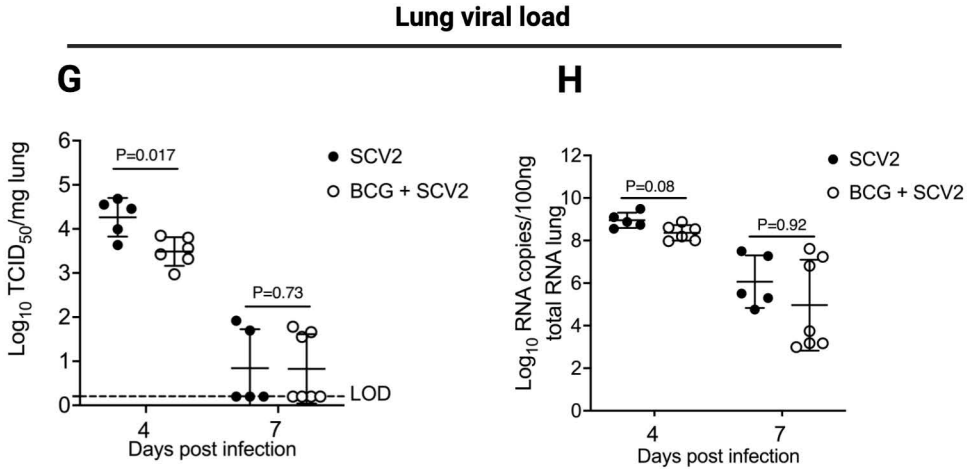

Figure 1. BCG vaccination diminishes SARS-CoV-2 (SCV2) infection induced lung inflammation and viral load in golden Syrian hamsters. A. Experimental layout. **B-C**. Bronchopneumonia at day 4 (D4) and day 7 (D7) after SARS-CoV-2 infection, mild local inflammation (arrows) in BCG + SCV2 lungs. Neutrophils **(D)** and macrophage **(E)** infiltration at D4 after SARS-CoV-2 infection. **F.** $CD3^+$ lymphocyte positivity scores at D4 in hamster lungs after SARS-CoV-2 infection. **G-H.** Bar graph showing SARS-CoV-2 viral load in the lung at D4 and D7 post infection in non-vaccinated and BCG-vaccinated hamsters. Briefly, Infective viral particles **(G)** were quantified from a standard of infectious virus and expressed at $TCID_{50}$ equivalents per mg lung tissues. Dotted lines indicate lower limit of detection (LOD). Viral RNA levels (H) were determined in the lungs, normalized against human RNaseP and were transformed to estimate viral RNA copies per 100 ng of total lung RNA. Data points represent number of animals used per group. Statistical analysis was done using two-sided Fisher exact test **(C-E)**, Welch's t-test **(F)** or two-tailed Student's t-test **(G-H)** (significant when $P < 0.05$). Percent animals and 95% confidence intervals (CI) showing pathology were **(C)** bronchopneumonia in the BCG-SCV2 group at D4 0% (95% CI: 0, 45.9%), at D7 28.6% (95% CI: 36.7, 71.0%); **(D)** neutrophil infiltration in the BCG-SCV2 group at D4 50% (95% CI: 11.8, 88.2%); **(E)** macrophage infiltration in the BCG-SCV2 group 83.3% (95% CI: 35.9, 99.6%) and in the SCV2 only group at D4 60.0% (95% CI: 14.7, 94.7%). A schematic of CD3 positivity **(F)** is given in methods section.

Figure 2

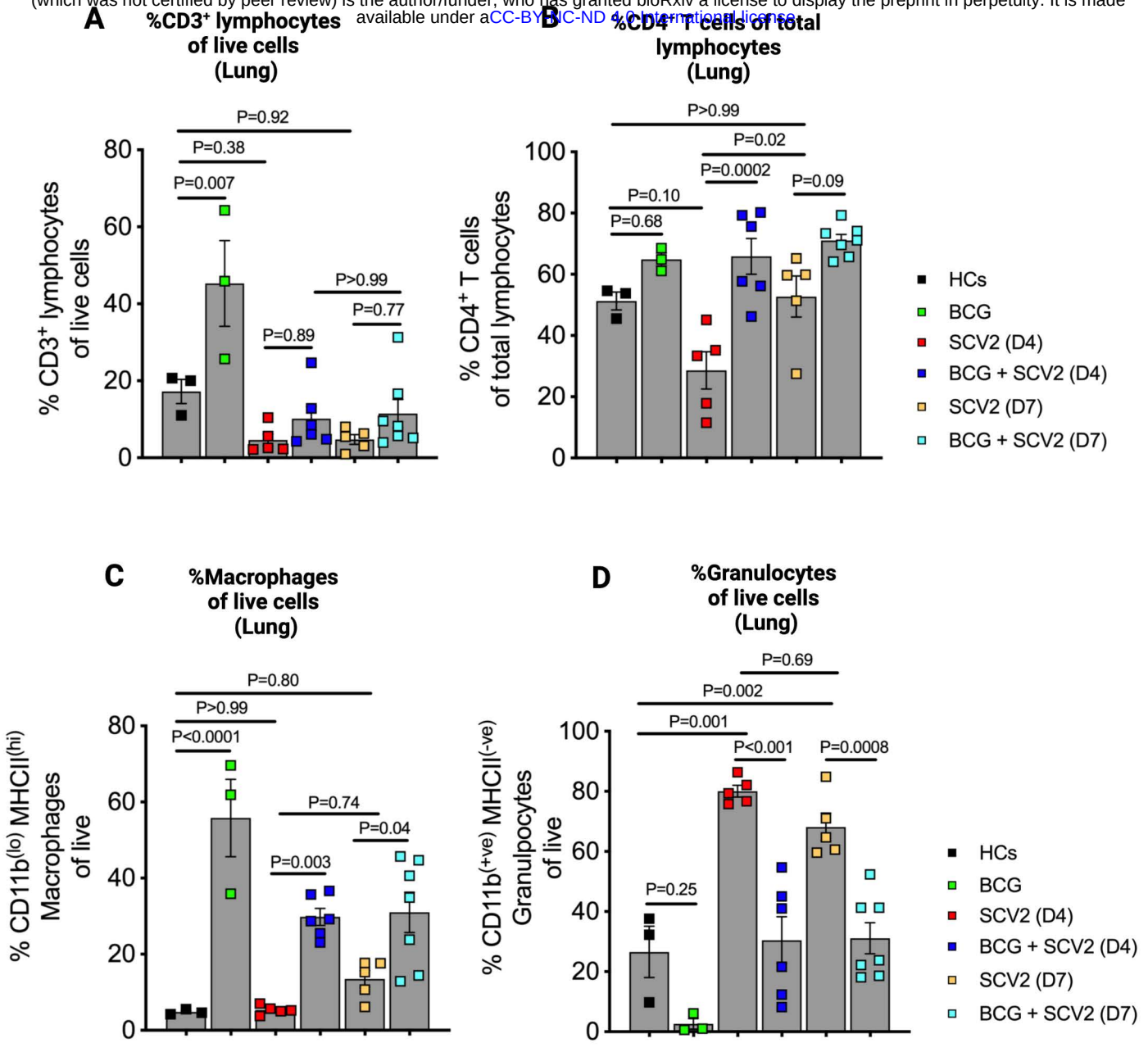

Figure 2. Differential abundance of lymphocytes, macrophages and granulocytes in BCG vaccinated golden Syrian hamster lungs after SARS-CoV-2 infection. Differential percentages of **A.** $CD3^+$ lymphocytes. **B.** $CD4^+$ T cells within the lymphocyte compartment. **C.** macrophages ($CD11b^{(lo)}$ $MHCII^{(hi)}$ of live cells) and, **D.** granulocytes ($CD11b^{(+ve)}$ $MHCII^{(-ve)}$ of live cells) in the lung of hamsters. Single cells preparations from lung tissues following necropsy were investigated for different lymphoid and myeloid cells using multicolor flow-cytometry. The data are presented as mean values ± S.E.M. Statistical analyses were done using one-way ANOVA with the p-values indicated.

Figure 3: scRNAseq of hamster lungs

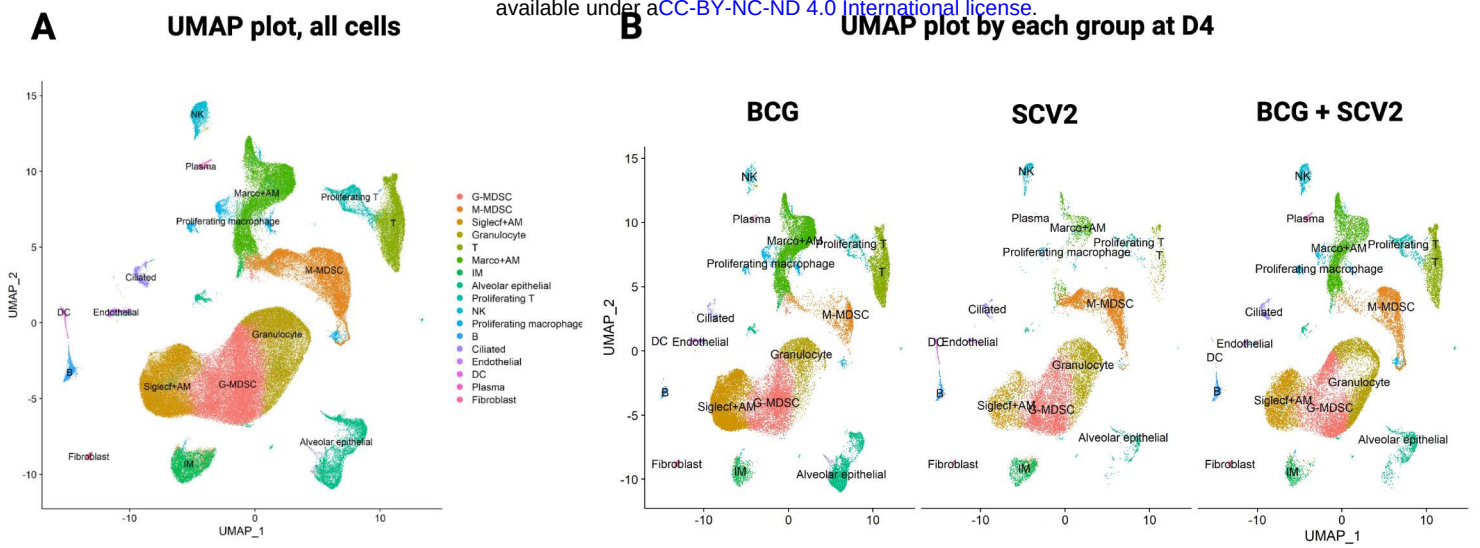

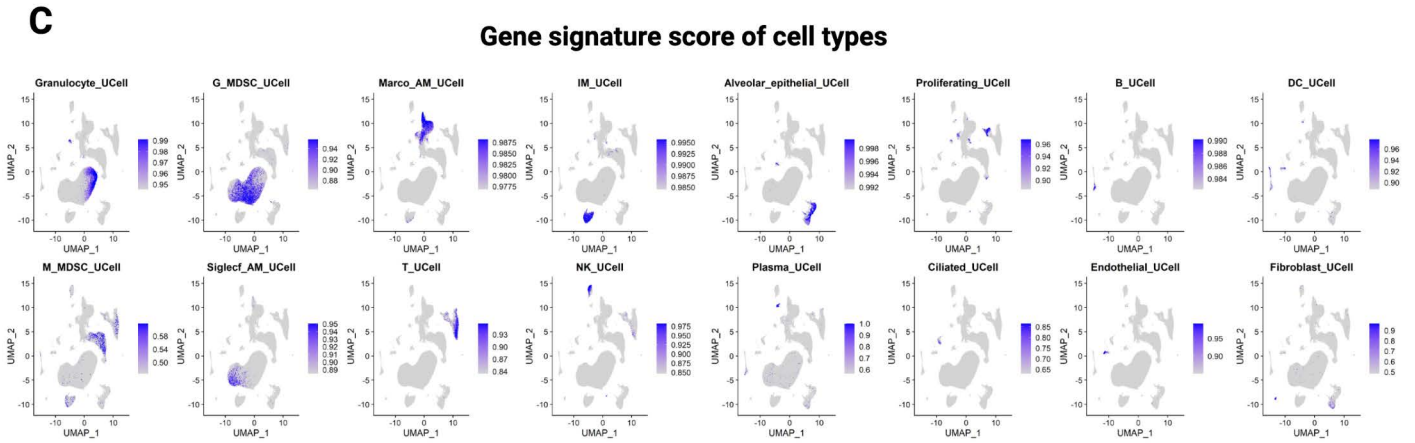

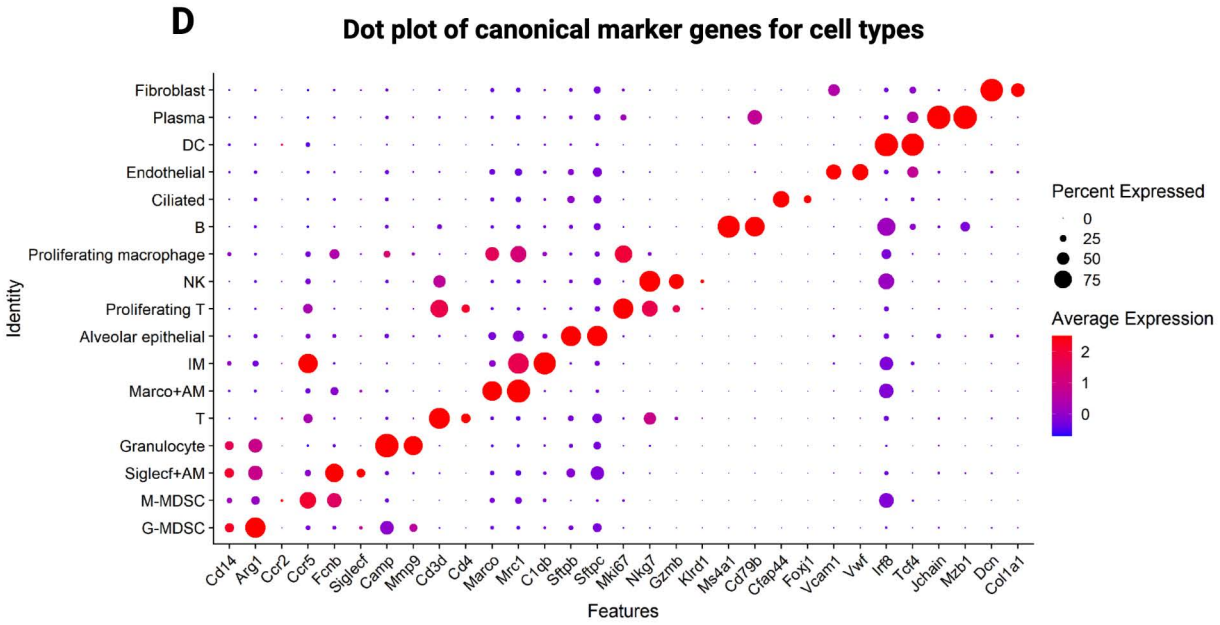

Figure 3. Cellular landscape of SARS-CoV-2 infected hamster lungs after BCG vaccination identified by scRNAseq. A. Uniform Manifold Approximation and Projection (UMAP) plot showing identification of 17 different major cell-types in hamster lungs integrated by all samples. **B.** UMAP plot showing lung cellular dynamics in hamster lungs in BCG vaccinated, SARS-CoV-2 (SCV2) infected, and BCG + SARS-CoV-2 (SCV2) infected animals at D4 after SCV2 infection. **C.** UCell score distribution in UMAP plot for cell type marker gene signatures (**listed in Table S2**) evaluated using UCell. **D.** Dot plots of log-normalized expression and fraction of cells expressing selected canonical marker genes for identification of 17 different cell types in hamster lungs across all samples.

Figure 4: Lymphoid cells

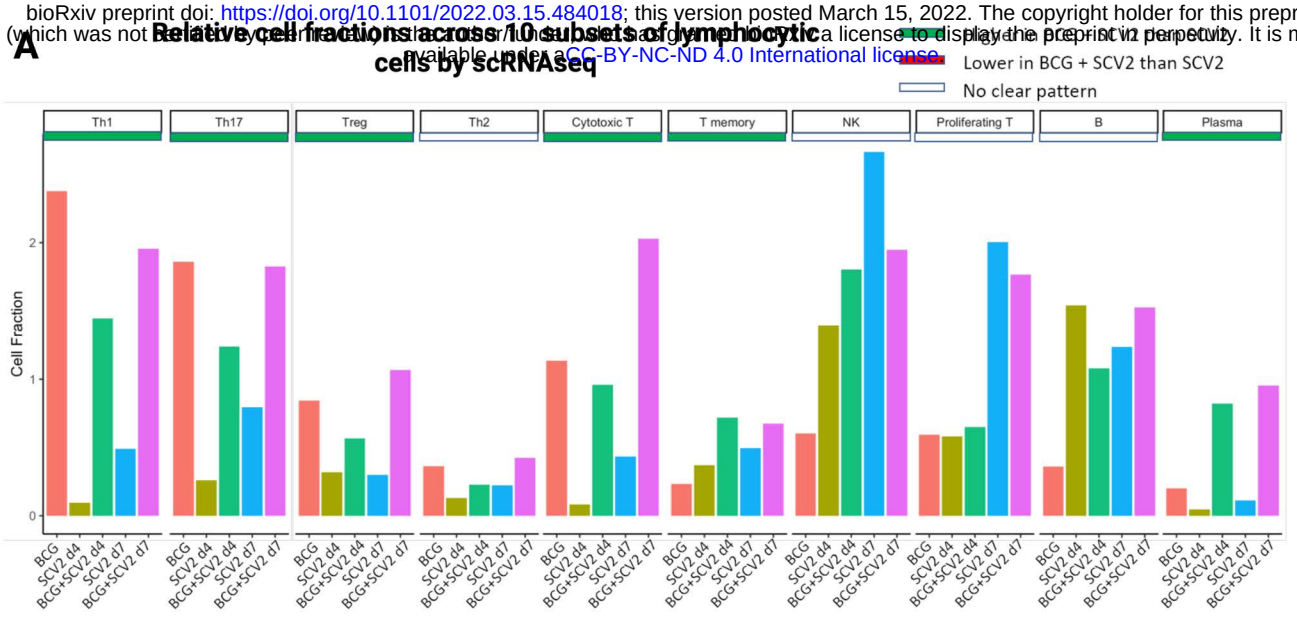

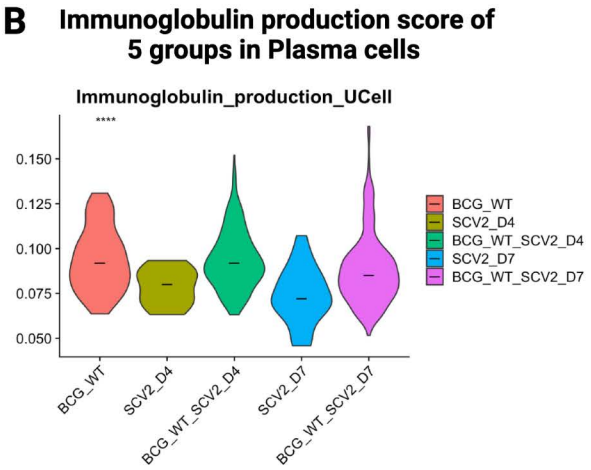

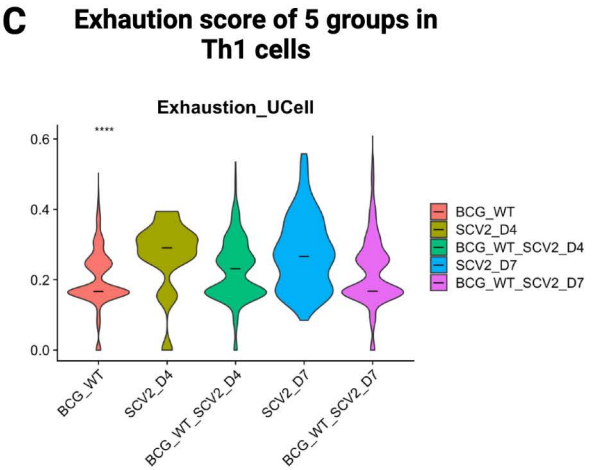

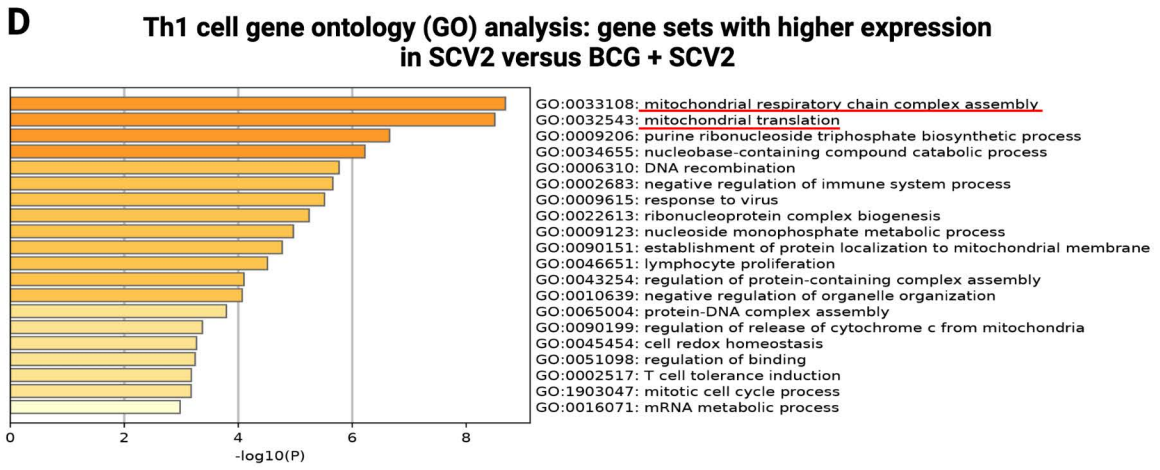

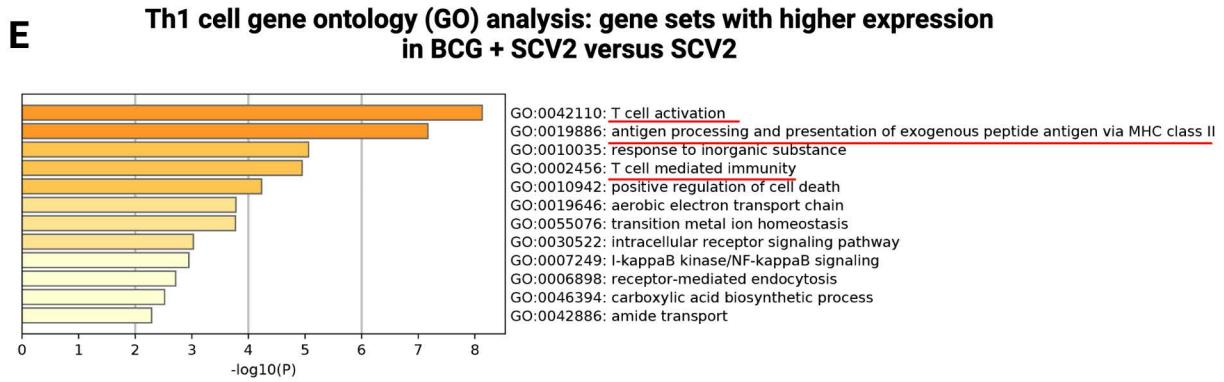

Figure 4 Lymphoid cells (continued)

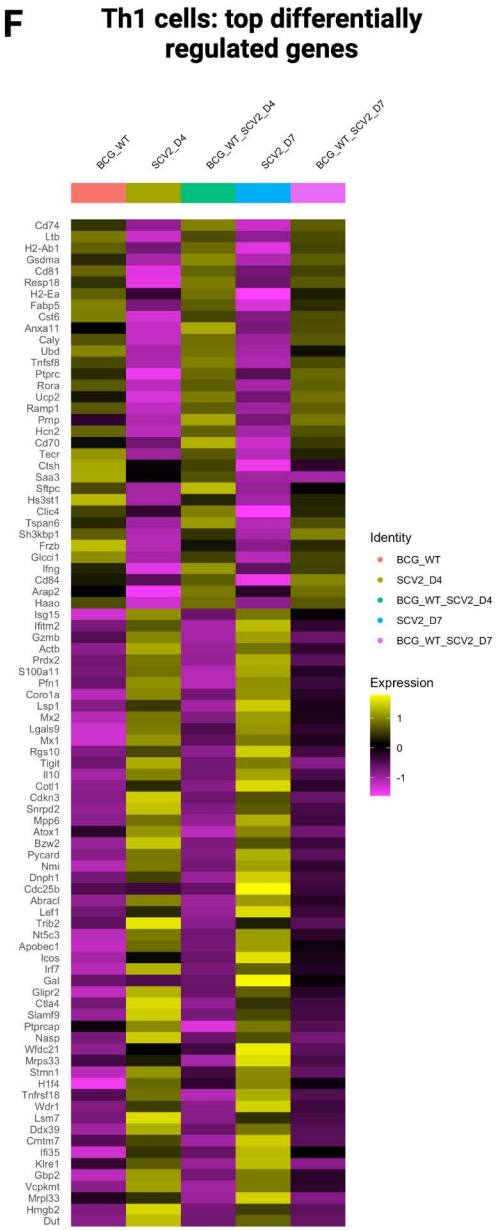

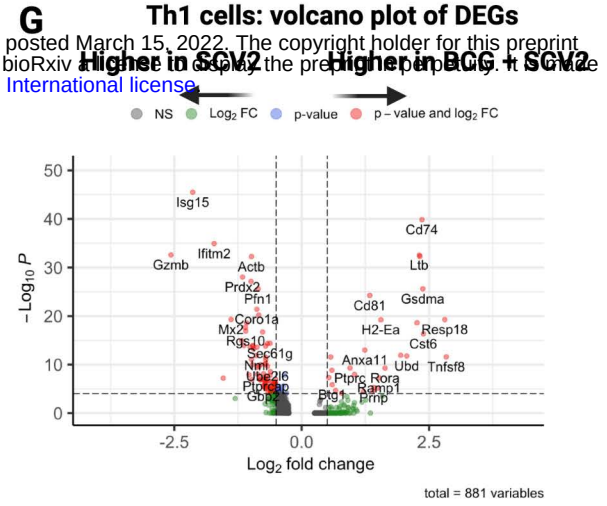

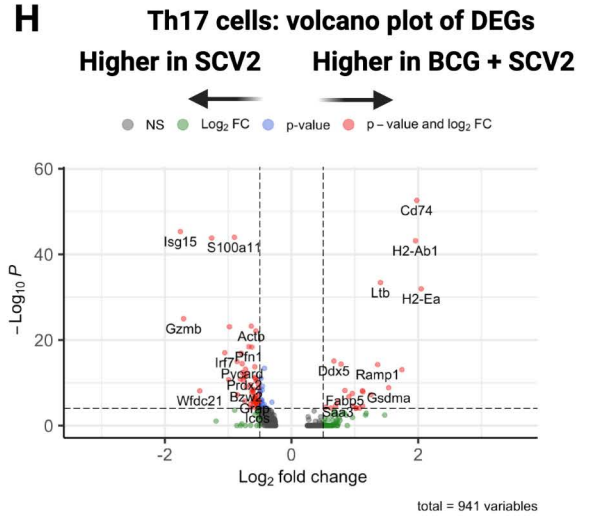

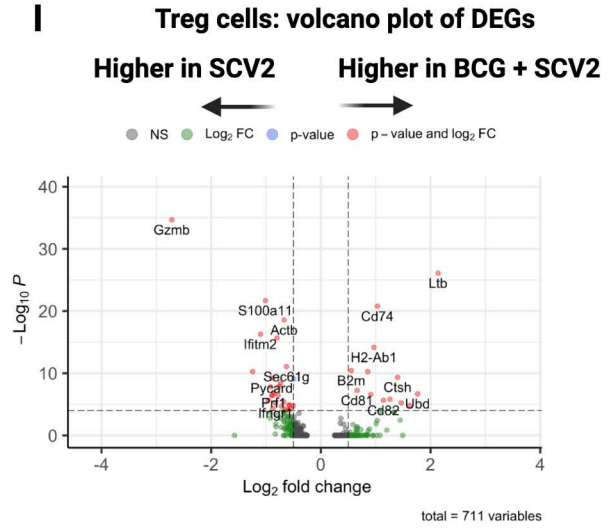

Figure 4. BCG vaccination strongly affects lung lymphoid dynamics and gene activation programs in different lymphoid subsets in SARS-CoV-2 infected hamster lungs. A. Bar graph showing average proportion of different lymphocytic cells across groups. Violin plots showing UCell scores for **(B)** immunoglobulin production on plasma cells, and **(C)** exhaustion scores on Th1 cells across different groups. Horizontal lines represent mean values. All differences with P < 0.01 are indicated. **P < 0.01, ***P < 0.001, ****P < 0.0001 (one-way ANOVA). Th1 lymphocyte-linked gene ontology enrichment analysis of biological processes showing gene sets that enriched in **(D)** SARS-CoV-2 (SCV2) versus BCG + SARS-CoV-2 (SCV2) and in **(E)** BCG + SARS-CoV-2 (SCV2) versus SARS-CoV-2 (SCV2) across both time-points. A darker color indicates a smaller P value. **F.** Heat map depicting the average expression value of top differentially expressed genes (DEGs) across different treatment conditions in Th1 cells. Top DEGs were selected with adjusted P-value < 0.05 and average fold change > 0.7. Volcano plots depicting DEGs in **(G)** Th1, **(H)** Th17, and **(I)** regulatory T cells (Tregs). The x-axis indicates log_2FC of gene expression in BCG + SCV2 compared to SCV2 group.

Figure 5: Myeloid cells

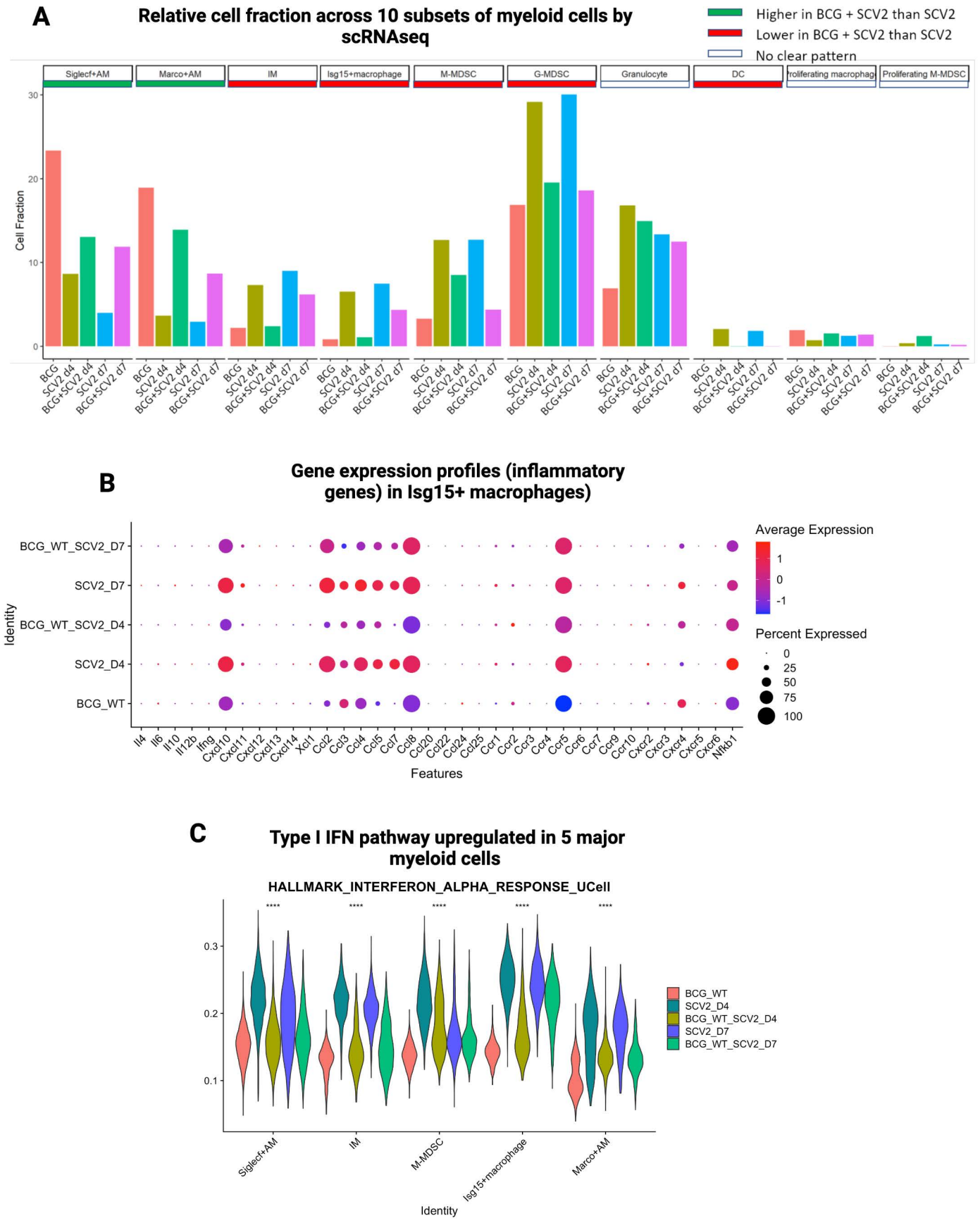

Figure 5 Myeloid cells (continued)

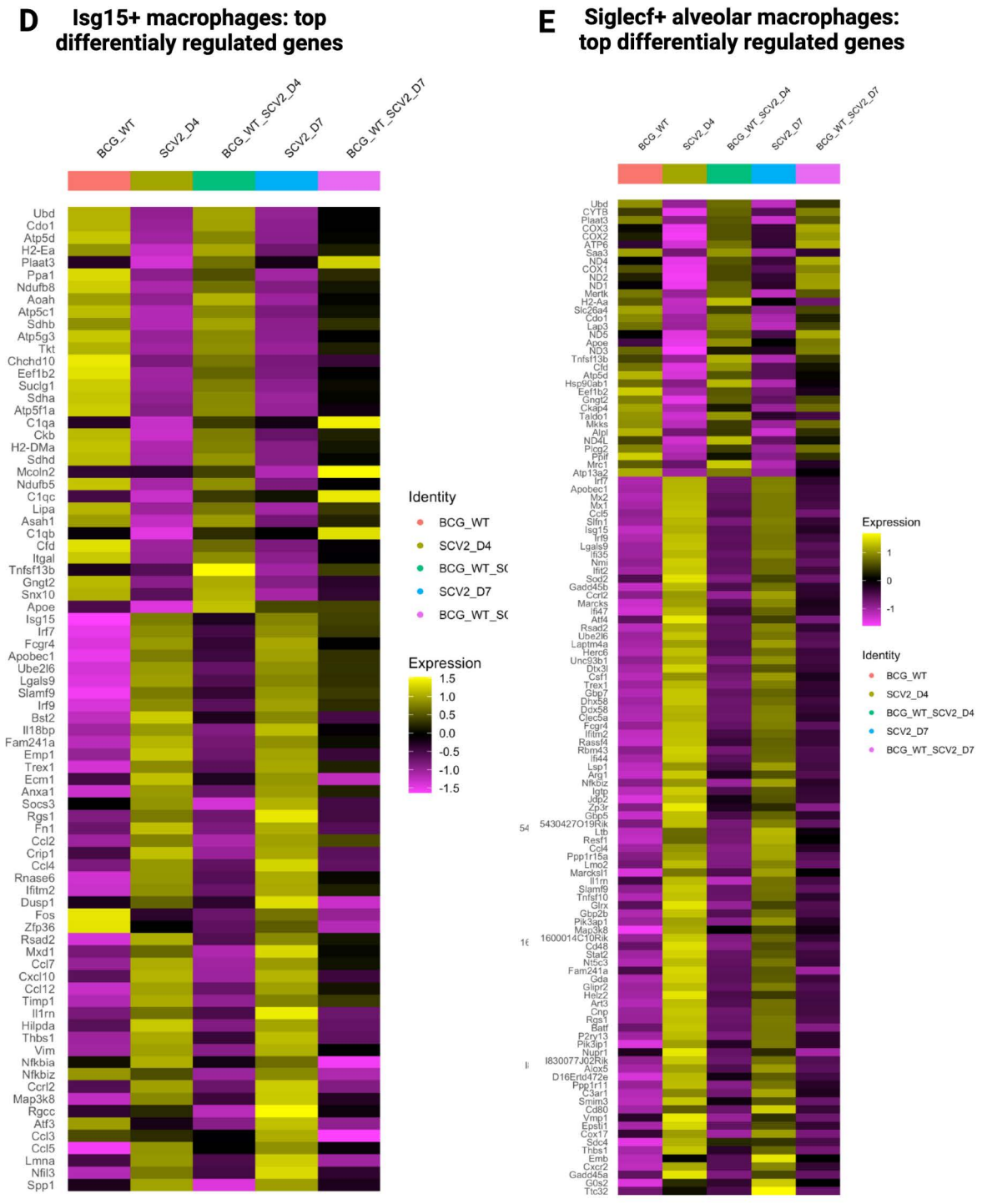

Figure 5. BCG vaccination curtails SCV2 mediated lung inflammation by modulating myeloid cell abundance and phenotypes. A. Bar diagram showing average proportion of different myeloid cells across groups. **B.** Dot plot showing the expression levels of a group of chemokines and cytokines in ISG15+ macrophages across different groups. **C.** Violin plots showing UCell gene signature scores of hallmark type I IFN (Interferon-α) responses in 5 major myeloid cells in hamster lungs across different groups. All differences with P < 0.01 are indicated. **P < 0.01, ***P < 0.001, and ****P < 0.0001 (one-way ANOVA). Heat map depicting the average expression value of top differentially expressed genes (DEGs) across different groups in **(D)** Isg15+ macrophages, and **(E)** Siglecf+ alveolar macrophages (AMs). Top DEGs were selected with adjusted P-values < 0.05 and average fold change > 0.7.

Figure 6: non-immune cells

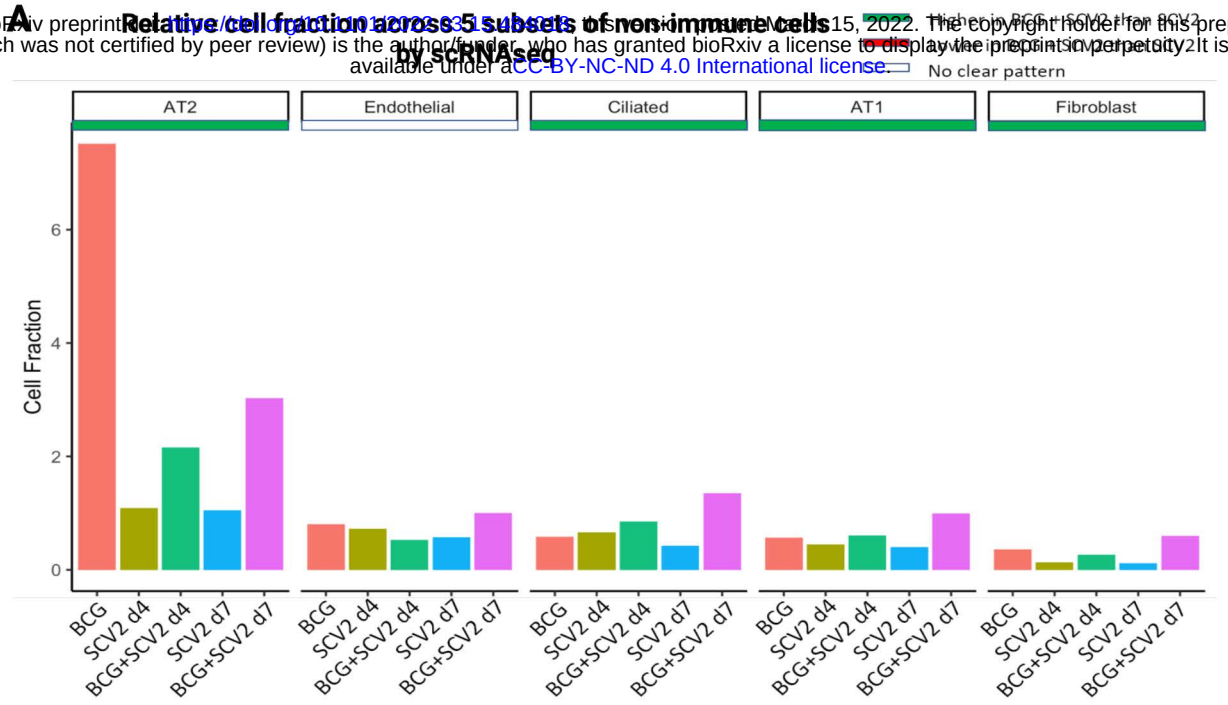

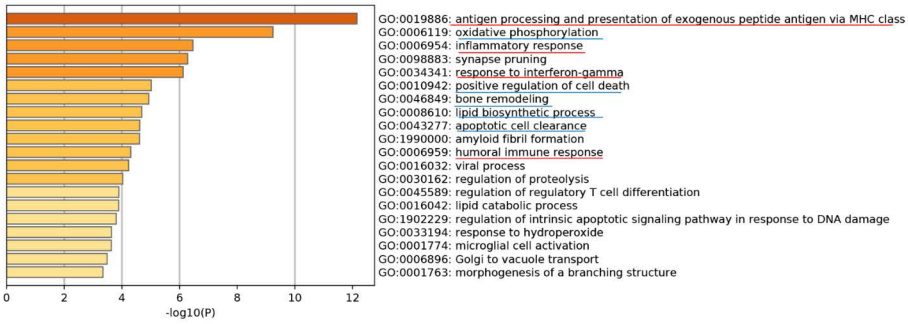

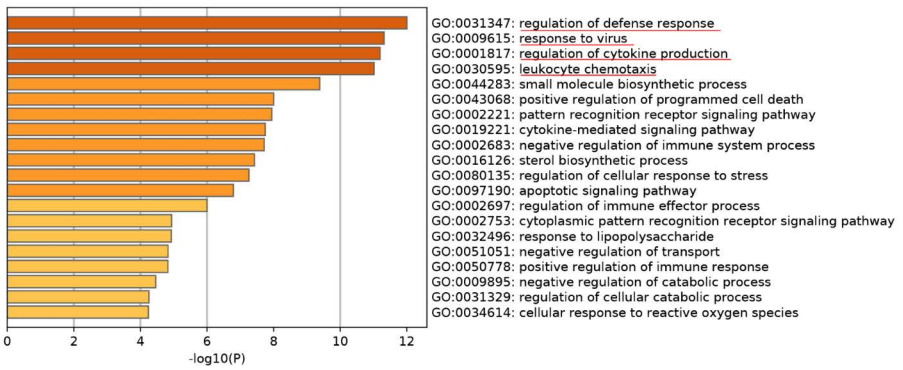

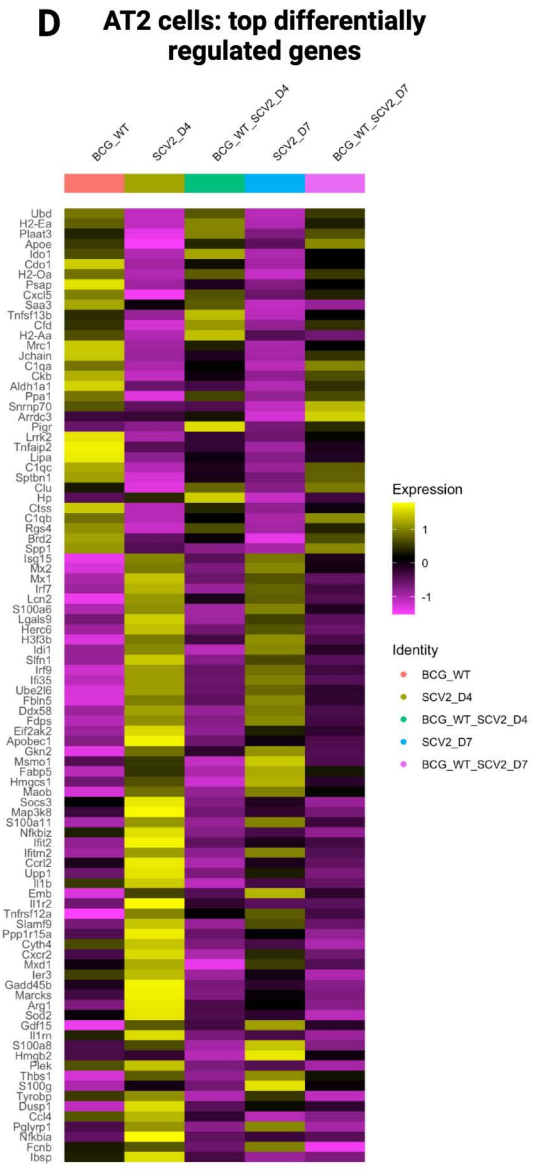

Figure 6. BCG vaccination restores AT2 cells and causes extensive phenotypic changes in non-immune cells in SARS-CoV-2 (SCV2) infected hamster lungs. A. Bar graph showing average proportion of different **(continued)...**

Figure 6 Continued.

lung non-immune cells across groups. AT2 cell-linked gene ontology enrichment analysis of biological processes showing gene sets that enriched in **(B)** BCG + SARS-CoV-2 (SCV2) versus SARS-CoV-2 (SCV2), and in **(C)** SARS-CoV-2 (SCV2) versus BCG + SARS-CoV-2 (SCV2) across both time-points, and **D.** heat map depicting the average expression value of top differentially expressed genes (DEGs) across different groups in AT2 cells. Top DEGs were selected with adjusted P-value < 0.05 and average fold change > 0.7.

Supplementary Figure S1

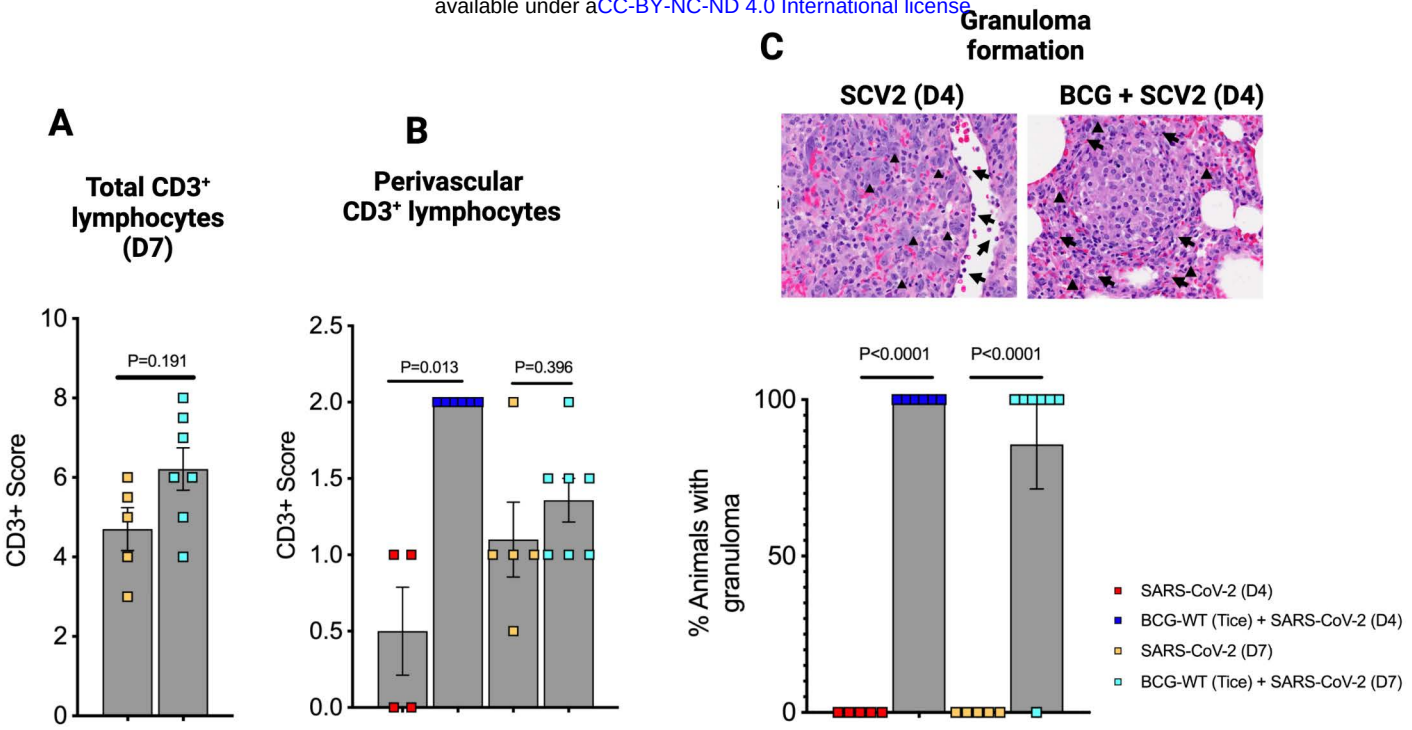

Supplementary Figure S1. Lymphocyte infiltration and granuloma formation in BCG vaccinated golden Syrian hmasters after SARS-CoV-2 infection. A. total CD3+ lymphocytes at day 7 (D7). **B.** CD3+ lymphocytes in perivascular area, and **C.** Granuloma formation and inflammation. Left panel showing HPF (200x) view of SARS-CoV-2 infected lungs showing alveolated parenchyma with marked pneumocyte atypia (arrowheads) acute inflammation (neutrophils showed by arrows) and breakdown of architecture sonsistent with acute lung injury secondary to pneumonia. Right panel HPF showing intraalveolar small non-necrotizing granuloma surrounded by abundant lymphocytes (arrowheads) and macrophages (arrows) in hamster lung at day 4 after SARS-CoV-2 challenge. Bar graph showing pathological quantification of granulomata after BCG vaccination. Data points represent number of animals per grouop. Data presented as mean values ± S.E.M. Statistical analyses done using Welch's t-test (P value < 0.05 considered significance). Schematic of CD3 positivity is given in methods section.

Supplementary Figure S2

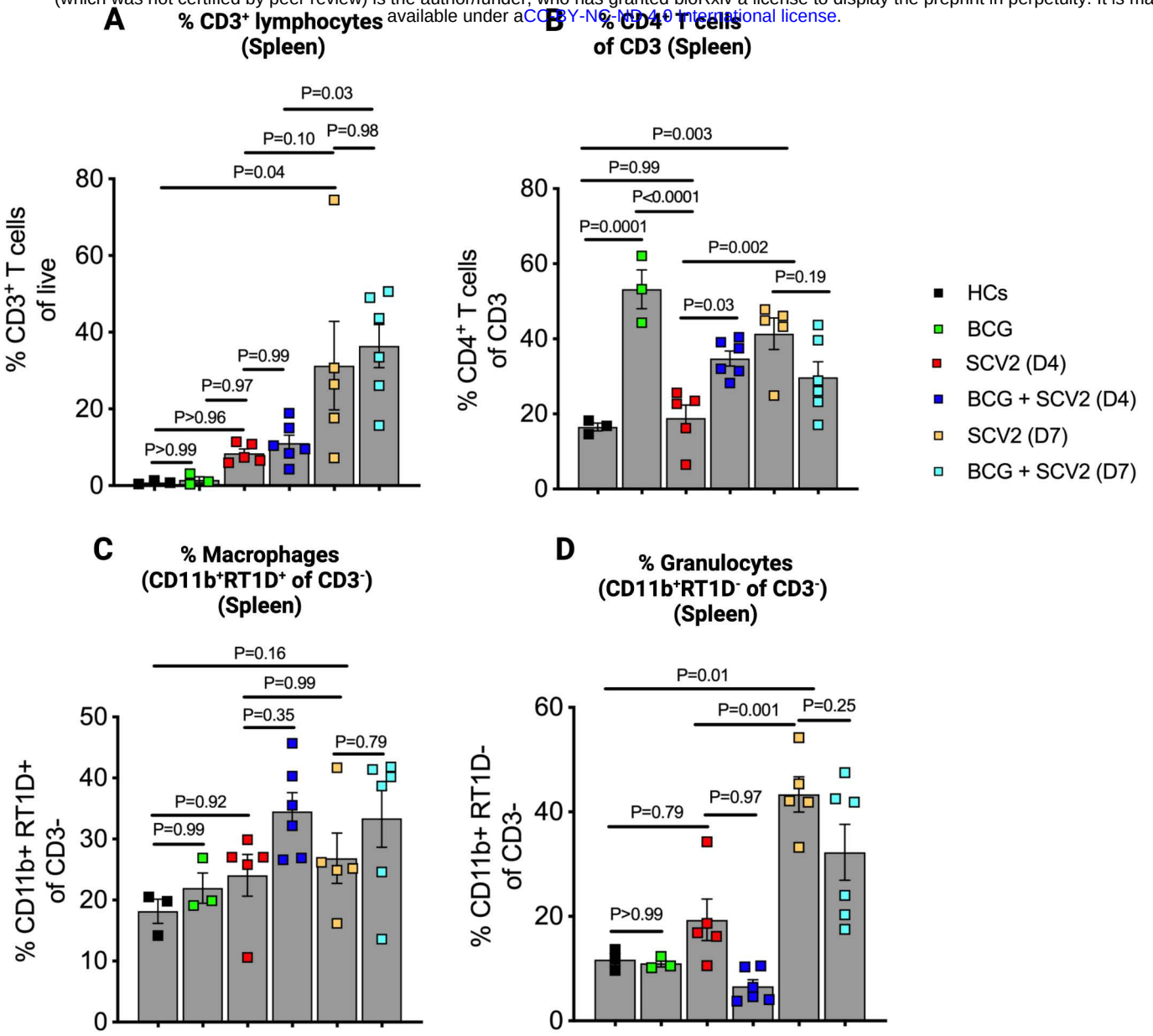

Supplementary Figure S2. Differential abundance of lymphocytes and myeloid cells in hamster spleens across different groups. Bar graph showing percentages of A. total lymphocytes ($CD3^+$). **B.** $CD4^+$ T cells within lymphocytic compartment ($CD4^+$ of CD3). **C.** macrophages ($CD11b^+RT1D^+$ of CD3-), and **D.** granulocytes ($CD11b^+RT1D^-$ of $CD3^-$) within non-lymphocytic compartment. Data points represent the number of animals assigned per group. Data are represented as mean values ± S.E.M. The statistical analyses were done using one-way ANOVA (P values <0.05 was considered significant).

Supplementary Figure S3

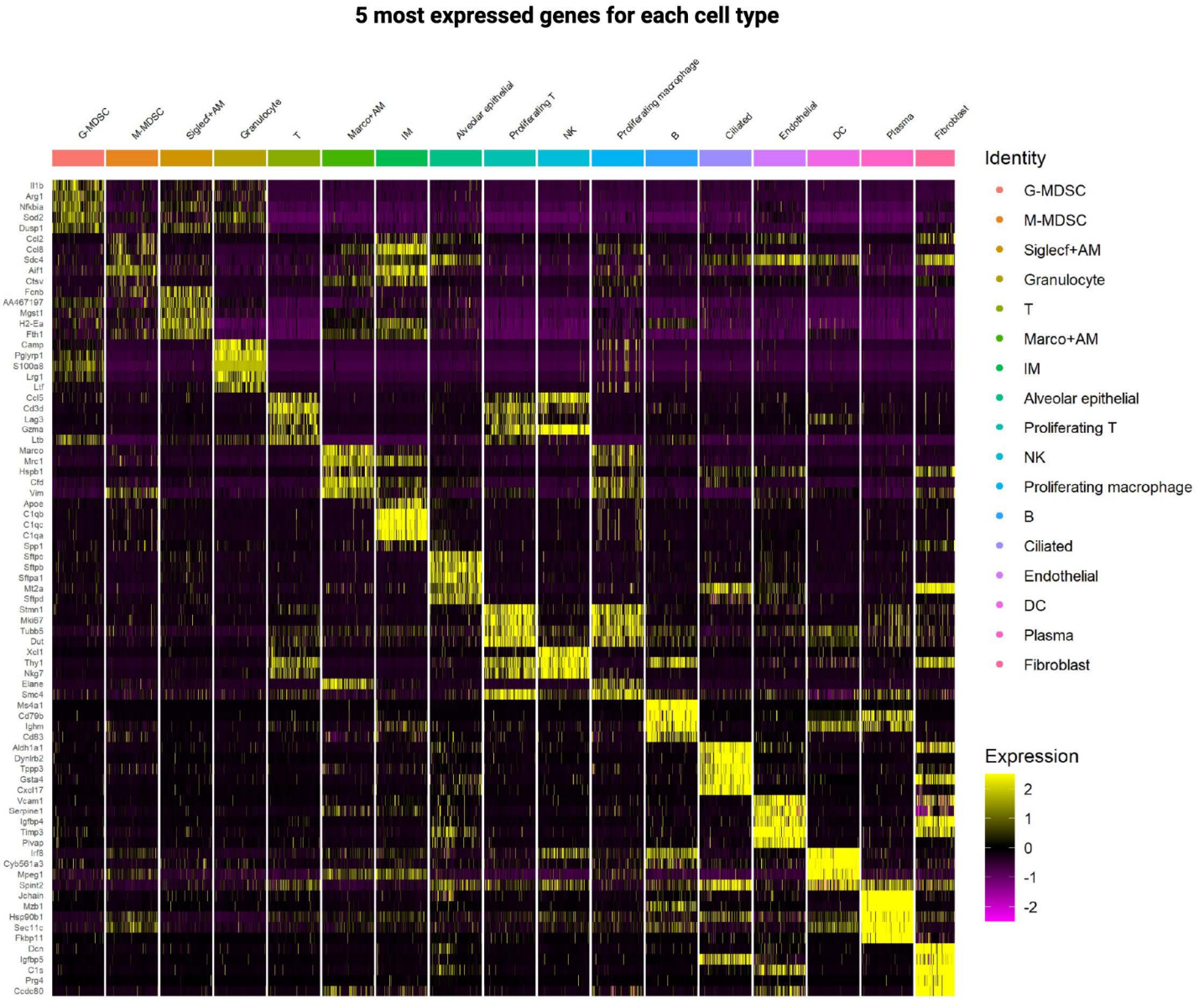

Supplementary Figure S3. Heat map showing top 5 most upregulated genes across 17 cell types identified within immune (myeloid and lymphoid) and non-immune cells using single cell RNA sequencing (scRNAseq) analysis.

Supplementary Figure S4

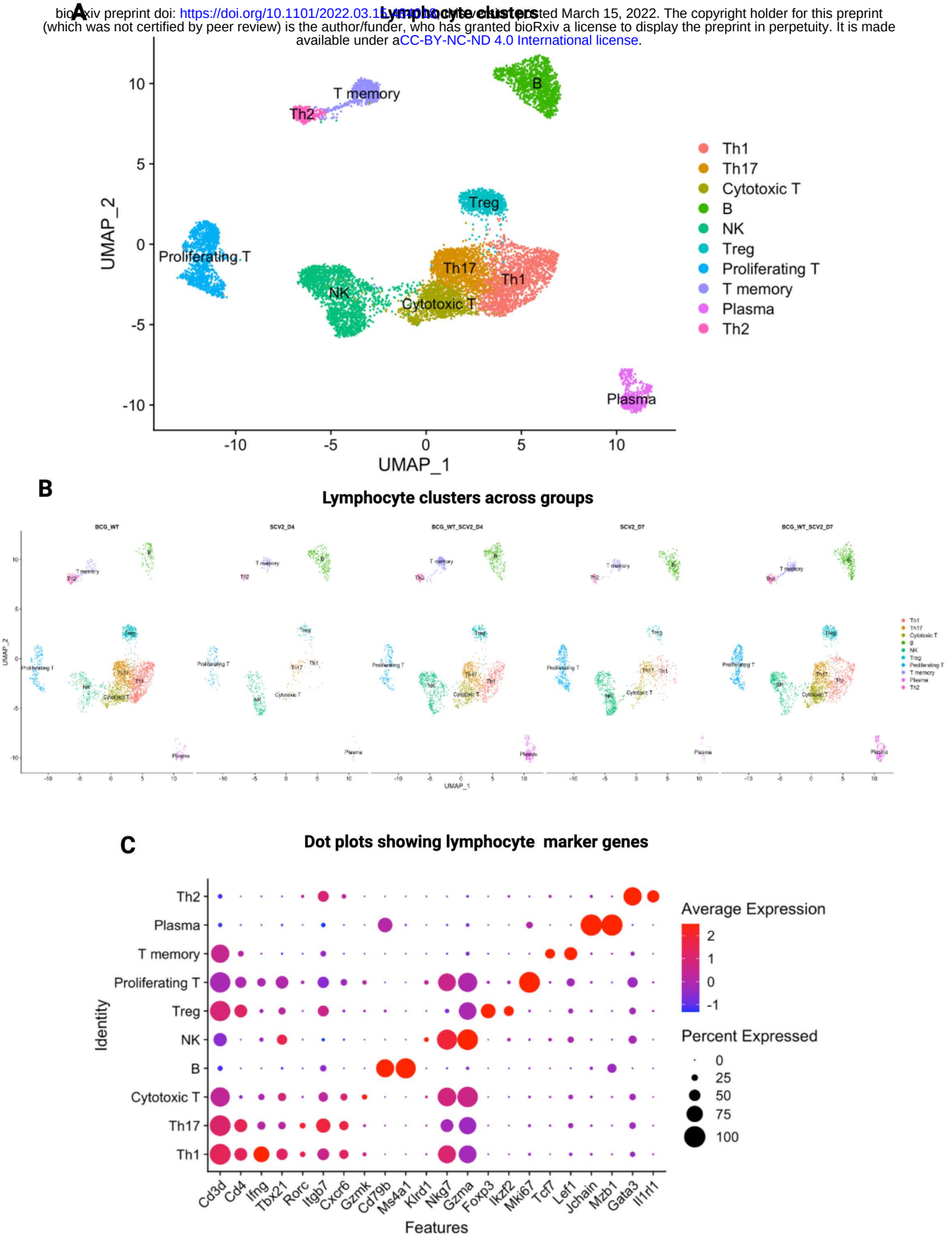

Fig S4 Lymphoid cells (continued)

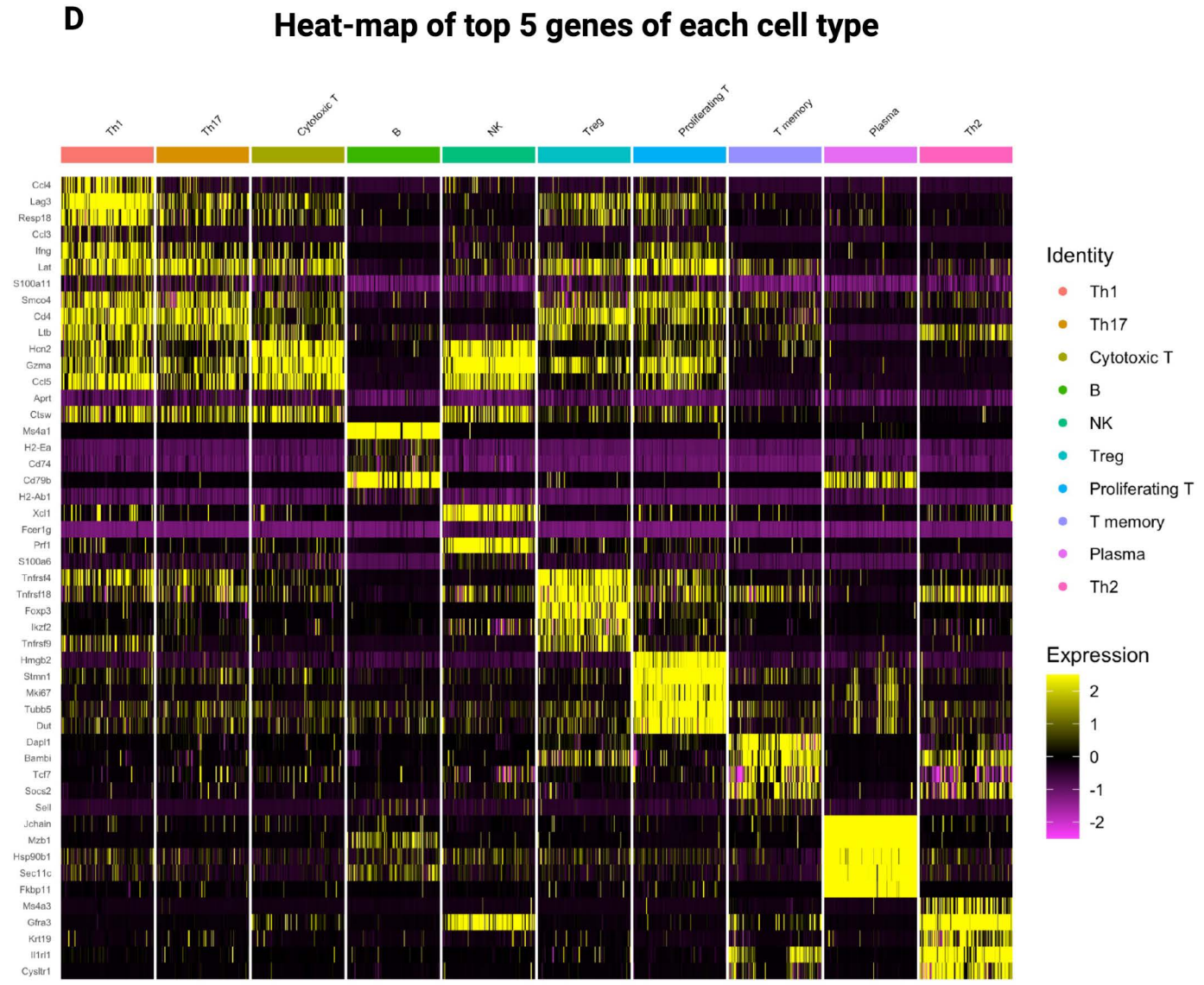

Supplementary Figure S4. Identification of different lymphocytic sub-set of cells across groups. A. Uniform Manifold Approximation and Projection (UMAP) plot showing 10 lymphocytic sub-sets using the cognate markers. **B.** UMAP plot showing dynamic changes in abundance of different lymphocytic cells across groups at both time points. **C.** Dot plot showing average expression of markers genes used to assign cellular identity, and **D.** Heat map showing top 5 genes expressed in different lymphoid subsets.

Supplementary Figure S5

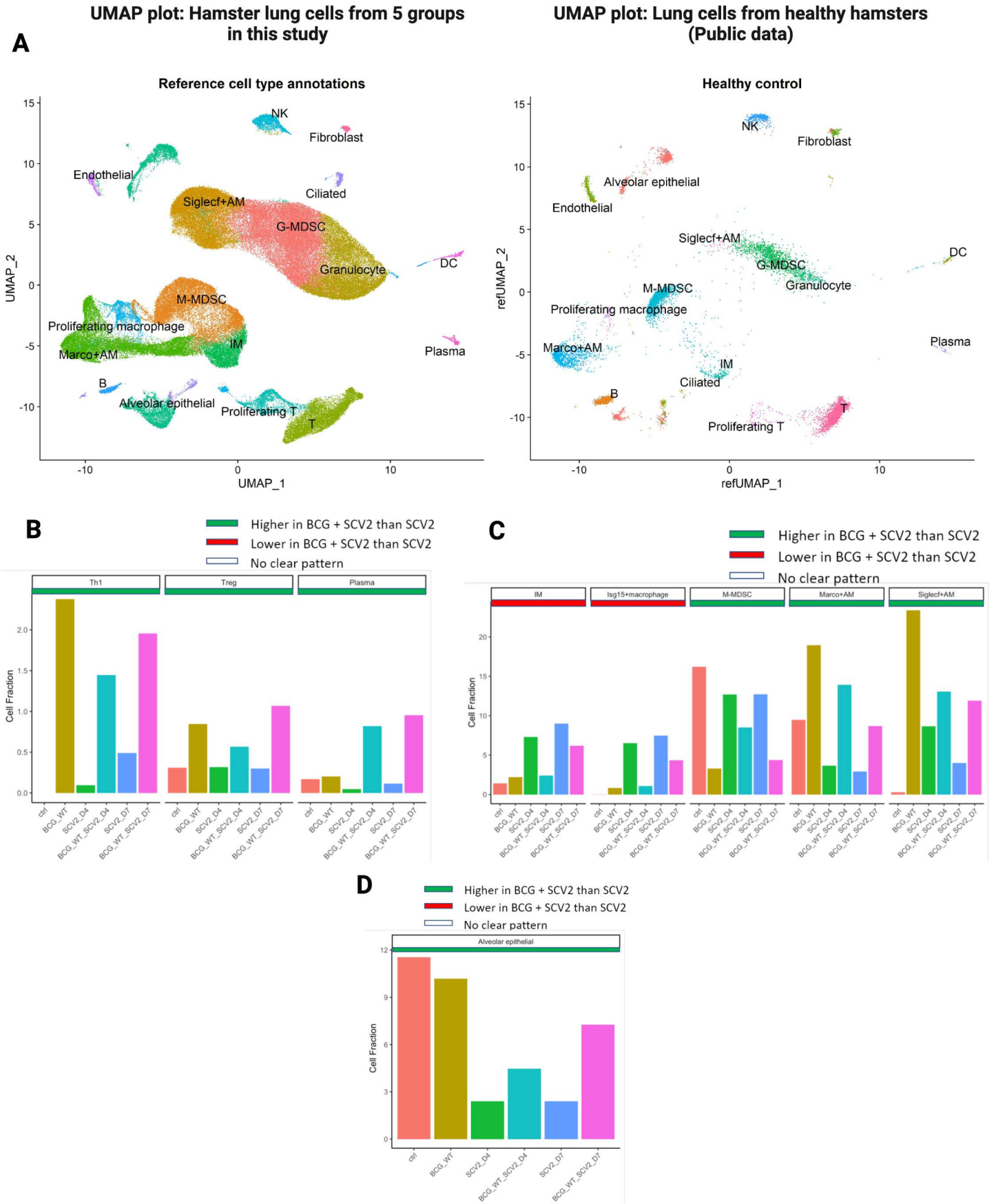

Supplementary Figure S5. BCG vaccination induced remodeling of myeloid cells in animal lungs after SARS-CoV-2 infection. A. Uniform Manifold Approximation and Projection (UMAP) plot showing different myeloid cells in hamster lungs after SCV2 infection (this study) and in healthy age-matched hamsters (without SCV2 infection, public database). Average proportion of **B.** Th1, Treg and plasma cells. **C.** Major myeloid subsets, and **D.** Alveolar epithelial cells in hamster lungs across different groups.

Supplementary Figure S6

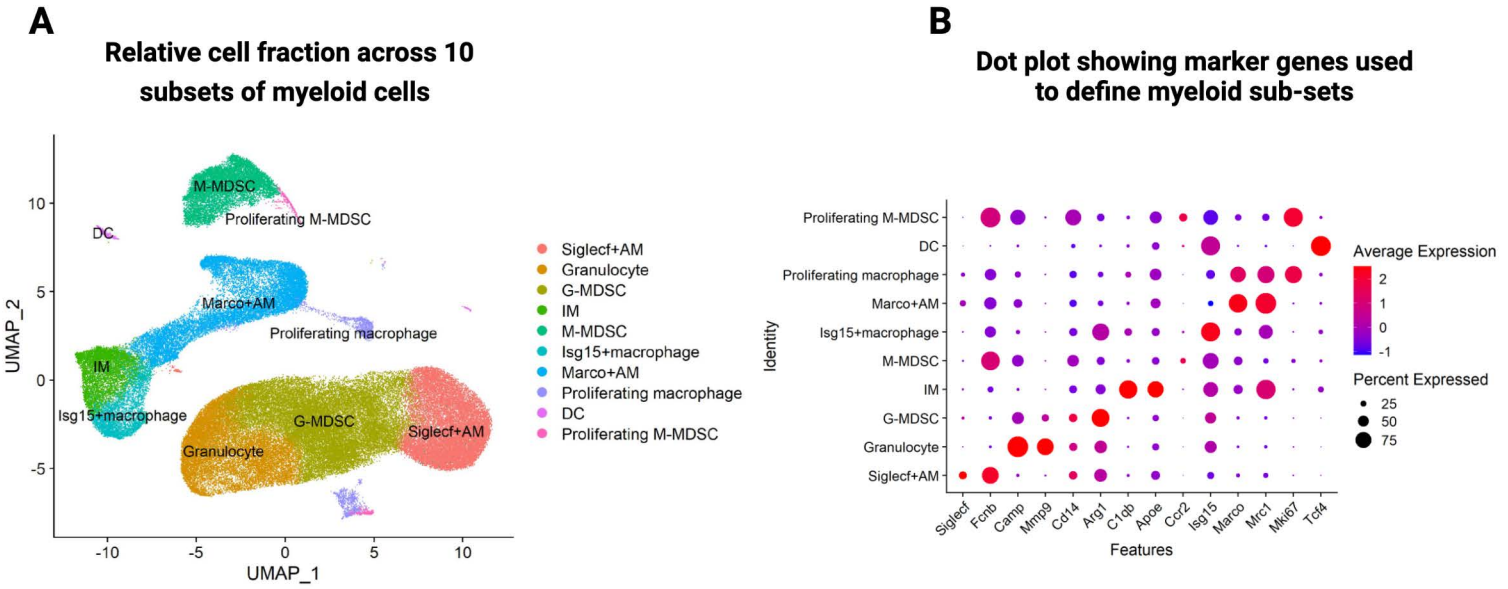

Supplementary Figure S6. Identification of different myeloid sub-sets of cells across all samples. A. Uniform Manifold Approximation and Projection (UMAP) plot showing different myeloid subset of cells integrated across all samples. **B.** Dot plot showing average expression and percentage cells expressing marker genes used to define different myeloid sub-sets.

Supplementary Figure S7

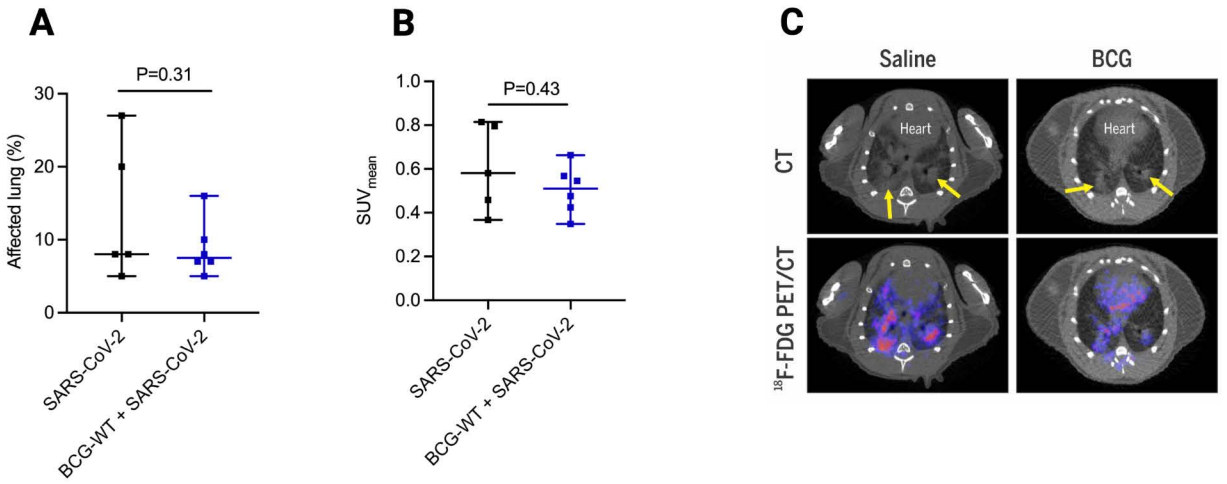

Supplementary Figure S7. Monitoring lung pneumonia in hamsters infected with SARS-CoV-2 using ^{18}F-FDG PET/CT. **A.** The affected lung areas were determined for each SARS-CoV-2-infected hamster using CT. Automated lung segmentation of the CT images was performed and data is represented as percentage of the lung determined to be affected based on tissue density. **B.** ^{18}F-FDG PET/CT was performed in SARS-CoV-2-infected hamsters. The ^{18}F-FDG PET signal in affected lung areas, as determined by the automated lung segmentation, was quantified, and is represented as mean standardized uptake value (SUVmean). The data is represented as median ± interquartile range. C. Transverse ^{18}F-FDG PET/CT of representative SARS-CoV-2-hamsters from the BCG-vaccinated and control groups. Increased ^{18}F-FDG PET signal was observed in the areas of lung consolidation observed in CT (yellow arrows).